A building-block strategy for dynamic anti-counterfeiting by using (Ba,Sr)Ga_2O_4:Sm^{3+} new red persistent luminescent phosphor as an important component

Ao Guo[a], Qi Zhu[a,*], Shimeng Zhang[a], Xudong Sun[b] and Ji-Guang Li[c,*]

[a]*Key Laboratory for Anisotropy and Texture of Materials (Ministry of Education), School of Materials Science and Engineering, Northeastern University, Shenyang, Liaoning 110819, China*

[b]*Foshan Graduate School of Northeastern University, Foshan, Guangdong 528311, PR China*

[c]*Research Center for Functional Materials, National Institute for Materials Science, Namiki 1-1, Tsukuba, Ibaraki 305-0044, Japan*

*Corresponding author

Dr. Qi Zhu

Tel: +86-24-8367-2700

E-mail: zhuq@smm.neu.edu.cn

Dr. Ji-Guang Li

Tel: +81-29-860-4394

E-mail: LI.Jiguang@nims.go.jp

Abstract

Long persistent luminescence materials developed to commercial standards are primarily concentrated in the blue and green regions, with only a few in the red region. Red, as one of the three basic colors, can be mixed in various proportions with blue and green to yield various colors. The development of red persistent phosphors has a broader application potential but remains a challenge. A solid-state reaction method was used to synthesize new red persistent luminescent materials of $Ba_{1-x}Sr_xGa_2O_4:Sm^{3+}$ (x = 0–0.09). In $BaGa_2O_4$, both Sr^{2+} and Sm^{3+} preferentially occupy the Ba^{2+} site rather than the Ga^{3+} site. When exposed to UV light at 254 nm, the phosphors emit the characteristic red emission of Sm^{3+} at wavelengths ranging from 500 nm to 750 nm. After removing the UV light source, an intense red afterglow that lasted more than 1400 seconds was observed. The red afterglow signal reappears after a heating process. Doping Sr^{2+} reduces the trap depth and improves the red persistent luminescence significantly. Because the escaped electrons from traps compensate for the emission loss of Sm^{3+} during the heating process, the red phosphors have unimaginably luminescent thermal stability. Thus, the emission intensity at 200 ˚C is 1.6 times that at room temperature. The prepared red persistent phosphors show multimode luminescence, with the output signal being time and temperature sensitive, indicating that they are potential luminescent materials for anti-counterfeiting applications. Finally, a building-block strategy for advanced anti-counterfeiting applications of dynamic display information is proposed, with red persistent phosphors serving as an important component combined with upconversion phosphors of $NaYF_4:Yb^{3+}$, Tm^{3+}, and green persistent phosphors of $SrAl_2O_4:Eu^{2+}$, Dy^{3+}.

Keywords:

Long persistent luminescence; Temperature-dependent luminescence; Anti-counterfeiting; $BaGa_2O_4$; Sm^{3+}

1. Introduction

There are some luminescent materials, that can continue to emit light for a certain period of time even after the external light source excitation is eliminated [1,2]. These materials are known as long persistent luminescence materials, and they are commonly used in places that require low lightings, such as night lights, traffic signs, and indoor safety escape signs [3,4]. They have recently been employed in radiation detection and optical storage media after adequate research and development [5,6]. Long persistent luminescent materials have been used in anti-counterfeiting, in vivo imaging, and medical diagnosis [7-10]. At the moment, materials with green and blue afterglow, such as $SrAl_2O_4:Eu^{2+}$, Dy^{3+} (green), and $CaAl_2O_4:Eu^{2+}$, Nd^{3+} (blue), have reached commercial standards, whereas red long persistent luminescence materials are difficult to attain these standards in terms of afterglow time and brightness [11,12]. Because red is one of the three basic colors, it can be mixed in various proportions with blue and green to produce various colors, giving it a broader application prospect [13-16]. Therefore, it is critical to developing red long persistent luminescence materials with superior properties.

Typically, emitting centers are critical for materials with persistent luminescence. The emitting color is always determined by the doped ions and the host materials. The host is fixed, but the doped ions can be changed. In other words, the afterglow color of the synthesized afterglow materials will be affected by the choice of different doped ions. When excited under certain conditions, Eu^{2+}, Eu^{3+}, Mn^{2+}, Sm^{3+}, or Pr^{3+} can produce red light [17-21]. Furthermore, through energy transfer processing [22], the emitting color of persistent luminescence materials can be changed because energy transfer from one ion to another doped ion during afterglow decay contributes to another afterglow, including red afterglow. This type of red long persistent luminescence was discovered in $Sr_3MgSi_2O_{8-1.5x}N_x:Eu^{2+},Dy^{3+},Mn^{2+}$, and $BaMg_2Si_2O_7:Eu^{2+},Dy^{3+},Mn^{2+}$ [23,24]. However, the duration and brightness of the afterglow are short and dim. Red long persistent luminescence materials such as $Ca_2SnO_4:Sm^{3+}$, $Y_2O_2S:Sm^{3+}$, and $Sr_2SnO_4:Sm^{3+}$ have been studied recently [25-27].

The typical transition between Sm^{3+} electronic configurations has been reported to contribute to a strong red emission [28]. As a result, Sm^{3+} is always used in red phosphors and red long persistent luminescence materials.

In addition to being influenced by doped ions, the intensity and duration of the persistent afterglow are determined by phosphor traps [29]. When the excitation is stopped, the trapped electrons or holes will be released to the emitting centers via the conduction or valence bands. It is believed that the traps are related to defects. Li et al. discovered a novel red-orange-emitting phosphor, $BaGa_2O_4:Bi^{3+}$, with $BaGa_2O_4$ as the host [30]. Because of the efficient traps formed by defects during the formation of $BaGa_2O_4$, $BaGa_2O_4:Bi^{3+}$ exhibited a long afterglow at extremely low temperatures [31]. Furthermore, this phosphor has excellent thermal stability, as its integrated intensity at 200 ˚C retains more than 88.1% of that at room temperature. As a result, this persistent luminescence material has promising applications in both extremely low and high-temperature conditions. As a result, $BaGa_2O_4$ could be used as a suitable host for long persistent luminescence phosphors.

Except for the host, the defects can be formed by doped ions occupying the site of host matrix ions with a different valence or ionic radius. A solid-state reaction method was used to synthesize $Ba_{1-x}Sr_xGa_2O_4:0.01Sm^{3+}$ (x = 0–0.09), a group of red persistent phosphors, with smaller Sr^{2+} substituting the larger Ba^{2+} to improve the persistent luminescence of $BaGa_2O_4:Sm^{3+}$. The samples were then characterized using XRD, UV-Vis, HRTEM, SAED, TL, PLE/PL spectroscopy, and persistent luminescence decay analysis. Finally, the possibility of their use in anti-counterfeiting applications was investigated.

2. Experimental section

2.1. Sample preparation

$Ba_{1-x}Sr_xGa_2O_4:0.01Sm^{3+}$ (x = 0, 0.01, 0.03, 0.05, 0.07, 0.09) samples, which are described as BGSO:Sm^{3+}, were synthesized by the high-temperature solid-state reaction method. $BaCO_3$, Ga_2O_3, Sm_2O_3, and $SrCO_3$ were chosen as the raw materials,

all purchased from Sinopharm (Shanghai, China) with a purity of 99.9%. Based on the stoichiometric ratio after calculation, all the raw materials were weighted by the electronic balance. The powders were ground for 30 min and then the mixture was calcined at 1400 ^{o}C for 8 hours. When cooling to room temperature, the powders were tested after ground again.

2.2. Characterization

The powder X-ray diffraction patterns were collected by X-ray diffraction (XRD, Model SmartLab, Rigaku, Tokyo, Japan) at the scanning rate of 8 min^{-1} in the 2θ range from 10^{o} to 70^{o}, operating at 40 mA and 40 kV using monochromated Cu Kα as radiation. The photoluminescence spectra (PL)/photoluminescence excitation spectra (PLE) of samples were obtained by the FP-8600 (JASCO, Tokyo) with a 150 W Xe-lamp as the excitation source. The diffuse reflectance spectra of the samples were acquired by a UV-vis spectrophotometer (UV-3600 Plus, Shimadzu, Kyoto, Japan). Long persistent luminescence spectra were recorded *via* the Horiba JY Fluorolog-3 (Kyoto) spectrofluorometer. An FJ-427A TL spectrofluorometer (Beijing Nuclear Instrument Factory, Beijing, China) at a heating rate of 1 K s^{-1} was used to gain Thermoluminescence (TL) curves after the samples were excited for 5 min by a UV lamp. In order to study the application in anti-counterfeiting, the commercial persistent phosphor of $SrAl_2O_4:Eu^{3+}$, Dy^{3+} (Luming Science and Technology Group Co., Ltd, China) was chosen here as a green light source. The afterglow luminance of sample was measured by a spectroradiometer (HS-1000, Photal Otsuka Electronics, Osaka, Japan) with a built-in software of the system.

3. Results and discussion

3.1. Synthesis and crystal structure

Fig. 1a depicts the XRD patterns of BGSO:Sm^{3+} (x = 0–0.09). All the XRD diffraction peaks are consistent with the standard patterns of $BaGa_2O_4$ (JCPDS NO. 46-0415), indicating the formation of a single phase of BGSO:Sm^{3+}. Because the ionic radii of Sm^{3+} (1.02 Å, CN = 7; 0.958 Å, CN = 6) and Sr^{2+} (1.21 Å, CN = 7; 1.18

Å, CN = 6) are close to that of Ba^{2+} (1.38 Å, CN = 7) and much larger than that of Ga^{3+} (0.47 Å, CN = 4), Sm^{3+} and Sr^{2+} ions are thought to substitute for Ba^{2+} sites. Furthermore, because the ionic radius of Sm^{3+} and Sr^{2+} is smaller than that of Ba^{2+}, the incorporation of Sm^{3+} and Sr^{2+} causes the shrink of lattice. The enlarged drawing of the (222) main diffraction peaks is show in Fig.1b. As the *x* value increases from 0 to 0.09, the (222) diffraction peak shifts to the higher angle side. This is primarily due to that smaller Sr^{2+} ions substitute the larger Ba^{2+} ions, causing the lattice to shrink. To test this inference, the Rietveld refinement results of the XRD pattern for BGSO (*x* = 0.07 sample) are analyzed and shown in Figure S1. The calculated results agree with the experimental data. The R_{wp}, R_p, and R_{exp} values are quite low, indicating that the results reliable. Interstitial oxygen is generated when Ba^{2+} ions are replaced by Sm^{3+} ions to compensate for the charge difference. This could contribute to long persistent luminescence.

The unit cell structure of $BaGa_2O_4$ is depicted in Fig. 2a. The hexagonal structure of $BaGa_2O_4$ belongs to the $P6_3$ space group. $BaGa_2O_4$ comprises six-membered ring layers of GaO_4 tetrahedra that are perpendicular to the *c*-axis, with its layers stacked to form a three-dimensional framework. Tunnels are formed by the superposition of the layers parallel to the *c*-axis, and the barium cations are in these tunnels. There are two types of barium ions: one with nine oxygen atoms located in a more symmetrical Ga-O tetrahedron six-membered ring, and the other with seven and eight oxygen atoms located in a more irregular Ga-O tetrahedron six-membered ring (Fig. 2b) [32]. Figures S2 and 2c show the FE-SEM and TEM morphology of BGSO:Sm^{3+} (*x* = 0.07) sample, indicating a particle size of 1–5 μm. The HRTEM image (Fig. 2c) and SAED patterns were examined (Fig. 2d). The HRTEM image's clear lattice fringes indicate that the sample has good crystallinity. The distance between the two crystal planes is about 0.325 nm. As a result, they correspond to the (411) crystallographic plane (d(411) = 0.32612 nm, JCPDS No. 46-0415). The calculated values of the diffraction spots, as shown in Fig. 2d, are approximately 0.325 nm, 0.352 nm, and 0.432 nm, which correspond to the (411), (410), and (00-1) planes, respectively (d(410) =

0.35216 nm, d(00-1) = 0.43326 nm, JCPDS No. 46-0415). The elemental distribution results in Fig. 2e-g show that Sr^{2+} and Sm^{3+} are successfully doped and that the chemical elements are homogeneously distributed.

3.2. Photoluminescence properties

Fig. 3a depicts the diffuse reflectance spectra of the BGSO (x = 0, 0.05, and 0.09) samples. The peak from 200 nm to 300 nm is attributed to the absorption of $BaGa_2O_4$ host [33]. The substitution of Sr^{2+} ions for Ba^{2+} sites did not affect the absorption. The Kubelka-Munk formula was used to calculate the band gap energy of the hosts [34]:

$$F(R) = \frac{(1-R)^2}{2R}$$

$$(\alpha h\nu)^2 = A(h\nu - E_g)$$

where R denotes the reflectivity of the sample, α denotes the absorption coefficient, which is proportional to $F(R)$, h denotes Planck's constant, ν denotes the light frequency, and A denotes the proportionality constant. The intercept of the diffuse reflection spectra transformed by the Kubelka-Munk function F(R) in Fig.3b can be used to calculate the bandgap energy. The bandgap of $BaGa_2O_4$ is approximately 5.01 eV. The band gap shrinks slightly as the Sr^{2+} doping content increase because the determined values are around 4.96 eV for x = 0.05 and x = 0.09 samples, which are smaller than 5.01 eV.

The PLE and PL spectra of $BaGa_2O_4$:0.01Sm^{3+} are shown in Fig.4a. The $O^{2-} \rightarrow Ga^{3+}$ charge transfer band is assigned to the strong band at 254 nm in the PLE spectra [33]. Because the host absorption of $BaGa_2O_4$ is close to the charge transfer band, the strong band could overlap the charge transfer band and the host absorption band. Sharp peaks ranging from 300 nm to 450 nm correspond to the Sm^{3+} intra-$4f^5$ transitions, with the $^6H_{5/2} \rightarrow {}^4K_{11/2}$ transition at 404 nm dominating [28]. The PL spectra obtained at an excitation wavelength of 254 nm show four narrow emission bands attributed to the $^4G_{5/2}$ to the $^6H_{5/2}$ (568 nm), $^6H_{7/2}$ (608 nm), $^6H_{9/2}$ (651 nm), and $^6H_{11/2}$ (707 nm) transitions of Sm^{3+}, with the sharp peak at 608 nm dominating [35,36].

The persistent luminescence spectra of $BaGa_2O_4$:0.01Sm^{3+} at room temperature are shown in Fig. 4b, which are nearly identical to the emission spectra of Sm^{3+}. When the sample is excited by a 254 nm UV light, four emission bands are observed at 568 nm, 608 nm, 651 nm, and 707 nm. Fig. 4c depicts the decay curve of persistent luminescence. A UV lamp was used to excite the sample for 5 min at room temperature. The red afterglow of the samples lasts more than 1400 seconds. The schematic energy level diagrams of $BaGa_2O_4$:0.01Sm^{3+} in Fig. 4d show the possible luminescence mechanism. The ground-state electrons of Sm^{3+} ions are promoted to the conduction band by UV irradiation. The excited states of Sm^{3+} are degenerated with free electron-hole states, with an electron at the bottom of the conduction band and a hole at the top of the valence band, because of the UV light excitation. Some excited electrons are delocalized in the CB and are captured by the GaO_4 tetrahedron. The electrons released from the GaO_4 tetrahedron to VB contribute to the blue emission [37], as evidenced by the host emission (Figure S3). Simultaneously, some electrons are relaxed to the excited levels of Sm^{3+} and relaxed to the $^4G_{5/2}$ level, and the energy relaxes through the transitions from $^4G_{5/2}$ to the $^6H_{5/2}$, $^6H_{7/2}$, $^6H_{9/2}$, and $^6H_{11/2}$ levels, contributing to the emission at 568, 608, 651, and 707 nm. Furthermore, the possible energy transfer from the GaO_4 tetrahedron to the $^4G_{5/2}$ energy level contributes to Sm^{3+} emission. When electrons are excited from the valence band to the conduction band by UV excitation, some electrons are captured and retained by the electron trap. During the illumination period, the electron traps are filled. When the ultraviolet irradiation excitation stops, the trapped electrons escape to the conduction band and then to the excited energy levels of Sm^{3+}, contributing to the afterglows [37, 38].

Electronic traps are critical for all long persistent luminescence materials. Shallow traps require less energy to allow captured electrons to escape more easily, comparing to deep traps. We used thermoluminescence (TL) to determine the trap depth of the samples. The TL glow curves for the samples as shown in Fig. 5a. The TL curves are not symmetrical, and there are two peaks in the TL curves corresponding to the shallow and deep traps, respectively. These two peaks are caused

by two different defects: charge compensation defects caused by Sm^{3+} replacing Ba^{2+} and the lattice distortion defects formed by the substitution of Sm^{3+} and Sr^{2+} for Ba^{2+}.

The trap depth can be calculated by the following equation [39]:

$$E = \frac{T_m}{500}$$

where T_m denotes the temperature for which the glow curve reaches a maximum, and E denotes the approximate trap depth. The trap depth for each sample is summarized in Table 1. The peaks of T_1 and T_2 shift to the lower temperature side as the x value increases, indicating that Sr^{2+} doping makes the traps shallower on the overall trend. Fig. 5b depicts the decay curves of persistent luminescence. A UV lamp was used to excite all the samples for 5 min at room temperature. The red afterglow in all samples lasts longer than 1400 seconds, because the afterglow luminance at 1400 s is estimated to be ~0.7–1.1 mcd/m^2, which is greater than the value of 0.32 mcd/m^2 [40]. Obviously, there are two types of laws for the decay curves at the initial and later parts. Increasing the x value from 0 to 0.07 results in a more intense afterglow for the initial duration (before 35 s), but increasing the x value from 0.07 to 0.09 results in a decline. However, for the later duration, a higher x value from 0 to 0.09 results in a more intense afterglow (after 35 s). This is because the intensity of the afterglow is affected by trap number and trap depth. The captured electrons can easily escape from the shallower traps, contributing to the stronger afterglow. Additionally, more electrons captured by more electron traps may contribute to a stronger afterglow. Because the x = 0.07 sample has the shallowest trap depth and the more trap number compared to the samples with x smaller than 0.07, it has the most intense afterglow at the initial stage. However, because of the larger electron trap numbers, the x = 0.09 sample exhibits a more intense afterglow than that for the x = 0.07 sample at the later stage. The results show that lattice distortion caused by substituting Ba^{2+} with Sr^{2+} can enhance the afterglow intensity.

Table 1 Calculated trap depths of BGSO:Sm^{3+} (x = 0, 0.05, 0.07, 0.09).

x	T_1	T_2	Trap I depth/eV	Trap II depth/eV
0	98	139	0.742	0.824
0.05	83	121	0.712	0.788
0.07	79	115	0.704	0.776
0.09	87	118	0.720	0.782

In Fig. 6a, the change in emission peaks can be observed with increasing heating temperature. In the case of BGSO:Sm^{3+} (x = 0.07), increasing the temperature yields an enhanced emission intensity under 254-nm UV lamp irradiation. The emission intensity at 200 ˚C is more than 160% of that at room temperature and about 80% of that at room temperature at 300 ˚C (Fig. 6b). The increased emission intensities are caused by captured electrons released from electron traps that combine with the excited state of Sm^{3+} by heat processing, which compensates for the emission loss caused by thermal quenching. This phenomenon was discovered previously in our research on $ZnGa_2O_4$:Cr^{3+} persistent luminescent materials [41,42]. Fig. 6c shows the persistent luminescence decay curves for the samples after 30 s of heating at 150 ˚C. Clearly, afterglow can be seen for all samples, with more intense afterglow found at a higher x value, which is nearly the same as that without heat processing. The afterglow intensity of the x = 0.07 sample, however, exhibits the fastest decline among the samples because it has the shallowest trap depth and the electrons are emptied most easily. As a result, the afterglow of the x = 0.07 sample is highly sensitive to temperature. The BGSO:Sm^{3+} (x = 0.07) sample was placed in cylindrical containers. As shown in Fig. 6d, as the temperature rises, the phosphors exhibit increased red emission when excited by 254-nm UV light. It can be seen that the emission intensity of BGSO:Sm^{3+} (x = 0.07) is the highest at 200 ˚C. Increasing the temperature further contributes to a decrease of the red signal. The luminescence mechanism after heat processing is depicted schematically in Fig. 6e. At elevated temperatures, the trapped electrons escape to the CB and combine with the excited energy levels of Sm^{3+}, which compensates for the emission loss caused by the thermal

quenching of Sm^{3+}. As a result, the intensity of the red emission increases after heating, and the sample exhibits a temperature-dependent luminescence.

3.3. Anti-counterfeiting applications

To investigate the anti-counterfeiting application, BGSO:Sm^{3+} (x = 0.07) and $NaYF_4$:Yb^{3+}, Tm^{3+} phosphors were mixed with a mass ratio of 1:1. The PL spectra and the appearance of the mixture phosphor under 980 nm laser excitation (2.5 W) are shown in Fig. 7a. The PL spectra show several emission bands corresponding to the $^1D_2 \rightarrow {}^3H_6$ (361 nm, purple), $^1D_2 \rightarrow {}^3F_4$ (450 nm, blue), $^1G_4 \rightarrow {}^3H_6$ (473 nm, blue), $^1G_4 \rightarrow {}^3F_4$ (646 nm, red), $^3F_2 \rightarrow {}^3H_6$ (695 nm, red), and $^3F_3 \rightarrow {}^3H_6$(723 nm, red) transitions of Tm^{3+} [43]. The images show that the mixture phosphor emits a blue upconversion light. The PL spectra and appearance of the mixture phosphor obtained after excitation at 254 nm are shown in Fig. 7b. Sm^{3+} also exhibits four narrow emission peaks at 568 nm, 608 nm, 651 nm, and 707 nm. The red emission of the mixture phosphors can be seen by the naked eye. The persistent luminescence spectra of the mixture phosphor at room temperature, which is assigned to the red afterglow of Sm^{3+}, are shown in Fig. 7c. The persistent luminescence decay curve of the mixture phosphor, which was excited by a 254 nm UV lamp for 5 min, is shown in Fig. 7d. The red afterglow from the mixture phosphor lasted more than 600 seconds.

The prepared samples could be successfully employed in advanced anti-counterfeiting applications due to their different emission performances at different exciting wavelengths. To capture the emission signals of the samples under different excitation conditions, the BGSO:Sm^{3+} (x = 0.07) sample and the mixture phosphor are placed in the "B" container fabricated by metal 3D printing (Fig. 7e). The phosphor 1 is BGSO:Sm^{3+} (x = 0.07), and the phosphor 2 is a mixture of the two. Under natural light, all the patterns are white "B". The four patterns showed bright red "B" and dark red "B" emissions at 254-nm UV excitation and after removing the 254-nm UV excitation lamp, respectively (Fig. 7e). The four patterns, however, exhibited blue "B", "p", "b", and "D" under 980-nm laser excitation.

BGSO:Sm^{3+} (x = 0.07) and $SrAl_2O_4$:Eu^{2+}, Dy^{3+} phosphors were mixed with weight ratios of BGSO:Sm^{3+} (x = 0.07) to $SrAl_2O_4$:Eu^{2+}, Dy^{3+} at 200:1 and 150:1, respectively. The PL spectra of the two phosphors mixtures obtained under excitation at 254 nm are shown in Fig. 8a. The PL spectra of the two mixture phosphors show four emission peaks from Sm^{3+} at 568 nm, 608 nm, 651 nm, and 707 nm, but the emission intensity of Sm^{3+} is weaker than that before mixing. The green emission of $SrAl_2O_4$: Eu^{2+}, Dy^{3+} is visible with the broadband at 515 nm [44]. The two emission intensities for the two mixed powders were compared. The $I_{(515)}/I_{(608)}$ ratio for the mixture with the weight ratio of BGSO:Sm^{3+} (x = 0.07) to $SrAl_2O_4$:Eu^{2+}, Dy^{3+} as 200:1 is approximately 0.6. However, $I_{(515)}/I_{(608)}$ is about 1.2 for the mixture with the weight ratio of BGSO:Sm^{3+} (x = 0.07) to $SrAl_2O_4$:Eu^{2+}, Dy^{3+} as 150:1. It implies that increasing the BGSO:Sm^{3+} content would cause the emission color shifting to the red range. The persistent luminescence spectra of the two mixture phosphors are shown in Fig. 8c. In the absence of 568 nm and 707 nm emission peaks for the phosphors mixture (the weight ratio of BGSO:Sm^{3+} to $SrAl_2O_4$:Eu^{2+}, Dy^{3+} is 200:1), afterglow emission peaks at 515 nm, 608 nm and 651 nm are observed, indicating that the afterglow is yellow. The persistent luminescence spectra of the mixture phosphors (weight ratio of BGSO:Sm^{3+} to $SrAl_2O_4$:Eu^{2+}, Dy^{3+} is 150:1) only has a 515-nm peak, and the Sm^{3+} emission peak disappears, illustrating that the afterglow is green. The relative intensities of 515 nm and 608 nm at different temperatures are shown in Fig. 8d, with the weight ratio of BGSO:Sm^{3+} (x = 0.07) to $SrAl_2O_4$:Eu^{2+}, Dy^{3+} of 150:1. As the temperature rises, the intensity of the green emission peak at 515 nm decreases steadily. It is worth nothing that the red emission of the mixture increases with an increased temperature. The red emission intensity of the mixture is highest at 150 ˚C, in contrast to that of BGSO:Sm^{3+}, which has the highest intensity at 200 ˚C.

The samples were placed in cylindrical containers labeled A, B, C, and D to capture the emission signal under different excitation conditions. In each condition, sample A emits red and sample D emits green, as shown in Fig. 9. With the increased content of $SrAl_2O_4$:Eu^{2+}, Dy^{3+}, the phosphors change color from red to green under the excitation of 254-nm UV light. In contrast, samples B and C show a color change

from red to yellow after 30 seconds of excitation. After 5 min of continuous excitation with 254 nm UV light, the sample emits an afterglow that changes from red to yellow and then to green with increased content of $SrAl_2O_4:Eu^{2+}$, Dy^{3+}. Sample B's afterglow is yellow, whereas the afterglow of sample C is green. The red-light emission of samples A, B, and C increases with increasing the heating temperatures. The green emission of sample D, however, decreases gradually.

Because the mixed phosphor demonstrated time- and temperature-dependent multimode luminescence, it has great potential in advanced anti-counterfeiting applications. Here, an apple tree logo was prepared using four powders as raw materials. Fig. 10 shows the images under 254 nm UV excitation and the afterglow images at room temperature. Under the excitation of 254-nm UV light, the three apples were red and ripe. After 30 seconds of excitation, apples B and C turned yellow and immature. The afterglow of apple B was also yellow, but the afterglow of apple C turned green. Under UV excitation at 254 nm, all three apples turned bright red at 100 ˚C and 200 ˚C. The red light from three apples became stronger, while the green glow from the tree trunk became weaker. At 300 ˚C, the light from trunk became more weaker, while the red light from the three apples weakened but remained bright.

4. Conclusion

Red long persistent luminescent materials of $Ba_{1-x}Sr_xGa_2O_4:Sm^{3+}$ (x = 0–0.09) were synthesized using a solid-state reaction method and characterized using XRD, UV-Vis, HRTEM, SAED, TL, PLE/PL spectroscopy, and persistent luminescence decay analysis. Both Sr^{2+} and Sm^{3+} preferentially occupy the Ba^{2+} site rather than the Ga^{3+} site in $BaGa_2O_4$. Doping with Sr^{2+} and Sm^{3+} does not significantly affect the crystal structure but causes lattice shrinkage and a narrower band gap. The samples exhibit characteristic Sm^{3+} emission with emission peaks ranging from 500 nm to 750 nm, belonging to $G_{5/2}$ to the $^6H_{5/2}$ (568 nm),$^6H_{7/2}$ (608 nm), $^6H_{9/2}$ (651 nm), and $^6H_{11/2}$ (707 nm) transition of Sm^{3+}. Doping Sr^{2+} reduces the trap depth and improves red

persistent luminescence significantly. The $Ba_{0.93}Sr_{0.07}Ga_2O_4:0.01Sm^{3+}$ sample exhibits the brightest and strongest red afterglow. Because the escaped electrons from traps compensate for the emission loss of Sm^{3+} during the heating process, the red phosphors have unimaginably luminescent thermal stability. The emission intensity at 200 ˚C is 1.6 times that at room temperature. The prepared red persistent phosphors exhibit time- and temperature-dependent luminescence, indicating that they could be used as multimode luminescent materials in anti-counterfeiting applications. Finally, a building-block strategy for advanced anti-counterfeiting applications is proposed, using the red phosphor as an important component combined with an upconversion phosphor and a green persistent phosphor.

Acknowledgments

This work was supported in part by the Natural Science Foundation of Liaoning Province (Grant 2020-MS-081), and National Natural Science Foundation of China (Grant 51302032, 51972047, 52172112).

References

[1] Y. Li, M. Gecevicius, J. R. Qiu, Long persistent phosphors-from fundamentals to applications, Chem. Soc. Rev. 45 (8) (2016) 2090-2136.

[2] D. Poelman, D. Van der Heggen, J. R. Du, E. Cosaert, P. F. Smet, Persistent phosphors for the future: Fit for the right application, J. Appl. Phys. 128 (24) (2020) 240903.

[3] T. Maldiney, C. Richard, J. Seguin, N. Wattier, M. Bessodes, D. Scherman, Effect of core diameter, surface coating, and PEG chain length on the biodistribution of persistent luminescence nanoparticles in mice, ACS. Nano. 5 (2) (2011) 854-862.

[4] R. Fu, Y. Y. Hu, H. N. Qiao, C. L. Yang, H. Yin, M. G. Ou, Luminescence property and magnetic resonance imaging of $Gd_2O_3:Tb^{3+}$ nanocrystals doped with Zn^{2+}, Li^{+}, Rare Met. 40 (8) (2021) 2049-2068.

[5] T. Maldiney, M. U. Kaikkonen, J. Seguin, Q. L. de Chermont, M. Bessodes, K. J. Airenne, S. Yla-Herttuala, D. Scherman, C. Richard, In vitro targeting of avidin-expressing glioma cells with biotinylated persistent luminescence nanoparticles, Bioconjug. Chem. 23 (3) (2012) 472-478.

[6] F. W. Kang, G. H. Sun, P. Boutinaud, H. Y. Wu, F. X. Ma, J. Lu, J. L. Gan, H. D. Bian, F. Gao, S. S. Xiao, Recent advances and prospects of persistent luminescent materials as inner secondary self-luminous light source for photocatalytic applications, Chem. Eng. J. 403 (2021) 126099.

[7] Z. J. Li, Y. W. Zhang, X. Wu, X. Q. Wu, R. Maudgal, H. W. Zhang, G. Han, In vivo repeatedly charging near-Infrared-Emitting mesoporous $SiO_2/ZnGa_2O_4:Cr^{3+}$ persistent luminescence nanocomposites, Adv. Sci. 2 (3) (2015) 1500001.

[8] T. Maldiney, B. T. Doan, D. Alloyeau, M. Bessodes, D. Scherman, C. Richard, Gadolinium-doped persistent nanophosphors as versatile tool for multimodal in vivo imaging, Adv. Funct. Mater. 25 (2) (2015) 331-338.

[9] J. F. Gao, J. H. Yang, X. Y. Zhang, J. Zhao, X. W. Liu, B. F. Shi, Synthesis and fluorescence properties of $CdTe:Eu^{3+}$ nanocrystals and core-shell SiO_2-coated $CdTe:Eu^{3+}$ nanospheres, Rare. Met. 38 (10) (2019), 989-995.

[10] Q. Q. Huang, H. Q. Gao, S. M. Yang, D. Ding, Z. H. Lin, Q. D. Ling, Ultrastable and colorful afterglow from organic luminophores in amorphous nanocomposites: advanced anti-counterfeiting and in vivo imaging application, Nano. Res. 13 (4) (2020) 1035-1043.

[11] T. Matsuzawa, Y. Aoki, N. akeuchi, Y. Murayama, New long phosphorescent phosphor with high brightness, $SrAl_2O_4:Eu^{2+}$, Dy^{3+}, J. Electrochem. Soc. 143 (8) (1996) 2670-2673.

[12] Y. H. Wang, L. Wang, Defect states in Nd^{3+}-doped $CaAl_2O_4:Eu^{2+}$, J. Appl. Phys. 101 (5) (2007) 053108.

[13] M. Allix, S. Chenu, E. Veron, T. Poumeyrol, E. A. Kouadri-Boudjelthia, S. Alahrache, F. Porcher, D. Massiot, F. Fayon, Considerable improvement of long-persistent luminescence in germanium and tin substituted $ZnGa_2O_4$, Chem. Mater. 25 (9) (2013) 1600-1606.

[14] A. Bessiere, S. Jacquart, K. Priolkar, A. Lecointre, B. Viana, D. Gourier, $ZnGa_2O_4:Cr^{3+}$: a new red long-lasting phosphor with high brightness, Opt. Express. 19 (11) (2011) 10131-10137.

[15] X. X. Qin, Y. Li, D. K. Wu, Y. L. Wu, R. C. Chen, Z. J. Ma, S. J. Liu, J. R. Qiu, A novel NIR long phosphorescent phosphor:$SrSnO_3:Bi^{2+}$, RSC. Adv. 5 (123) (2015) 101347-101352.

[16] C. Shi, X. Y. Shen, Y. A. Zhu, X. Q. Li, Z. Y. Pang, M. Q. Ge, Excitation wavelength-dependent dual-mode luminescence emission for dynamic multicolor anticounterfeiting, ACS. App. Mater. Inter. 11 (20) (2019) 18548-18554.

[17] D. D. Jia, Enhancement of long-persistence by Ce Co-doping in $CaS:Eu^{2+}$, Tm^{3+} red phosphor, J. Electrochem. Soc. 153 (11) (2006) H198-H201.

[18] H. M. Yang, J. Shi, M. L. Gong, A novel red emitting phosphor $Ca_2SnO_4:Eu^{3+}$, J. Solid. State. Chem. 178 (3) (2005) 917-920.

[19] L. Lin, M. Yin, C. S. Shi, W. P. Zhang, Luminescence properties of a new red long-lasting phosphor: $Mg_2SiO_4:Dy^{3+}$, Mn^{2+}, J. Alloy. Compd. 455 (1-2) (2008) 327-330.

[20] A. Mattner, L. Zimmermann, S. Lienenklaus, S. Weiss, C. Wickleder, Tailoring long lasting luminescence of red-emitting $CaWO_4:Eu^{3+}$, Sm^{3+} nanoparticles with enhanced crystallinity for improved bio-imaging, Ceram. Int. 46 (16) (2020) 26295-20298.

[21] L. Q. Yang, Z. Y. Cai, L. Q. Yang, J. Hu, Z. J. Zhao, Z. P. Liu, Solid state synthesis, luminescence and afterglow enhancements of $CaTiO_3:Pr^{3+}$ by Ga^{3+} codoping, J. Lumin. 197 (2018) 339-342.

[22] C. Rosticher, B. Viana, G. Laurent, P. Le Griel, C. Chaneac, Insight into $CaMgSi_2O_6:Eu^{2+}$, Mn^{2+}, Dy^{3+} nanoprobes: influence of chemical composition and crystallinity on persistent red luminescence, Eur. J. Inorg. Chem. (22) (2015) 3681-3687.

[23] J. Zhang, G. B. Chen, A long-persistent phosphor $Sr_3MgSi_2O_{8-1.5x}N_x:Eu^{2+}$, Dy^{3+}, Mn^{2+} based on white LEDs applications, J. Lumin. 211 (2019) 69-75.

[24] S. Ye, J. H. Zhang, X. Zhang, S. Z. Lu, X. G. Ren, X. J. Wang, Mn^{2+} activated red phosphorescence in $BaMg_2Si_2O_7:Mn^{2+}$, Eu^{2+}, Dy^{3+} through persistent energy transfer, J. Appl. Phys. 101 (6) (2007) 063545.

[25] Z. H. Ju, R. P. Wei, J. R. Zheng, X. P. Gao, S. H. Zhang, W. S. Liu, Synthesis and phosphorescence mechanism of a reddish orange emissive long afterglow phosphor Sm^{3+}-doped Ca_2SnO_4, Appl. Phys. Lett. 98 (12) (2011) 121906.

[26] B. F. Lei, Y. L. Liu, G. B. Tang, Z. R. Ye, C. S. Shi, A new orange-red long-lasting phosphor material $Y_2O_2S:Sm^{3+}$, Chem. J. Chinese U. 24 (2) (2003) 208-210.

[27] X. Yu, X. H. Xu, J. B. Qiu, Enhanced long persistence of $Sr_2SnO_4:Sm^{3+}$ red phosphor by co-doping with Dy^{3+}, Mater. Res. Bull. 46 (4) (2011) 627-629.

[28] Z. H. Wang, X. F. Shi, X. J. Wang, Q. Zhu, X. D. Li, B. N. Kim, X. D. Sun, J. G. Li, Enhanced hydrothermal crystallization and color tailorable photoluminescence of hexagonal structured YPO_4:Sm/Tb nanorods, Crys. Eng. Comm. 20 (17) (2018) 2357-2365.

[29] Y. Zhang, R. Huang, H. L. Li, D. J. Hou, Z. X. Lin, J. Song, Y. Z. Guo, H. H. Lin, C. Song, Z. W. Lin, J. Robertson, Germanium substitution endowing Cr^{3+}-doped zinc aluminate phosphors with bright and super-long near-infrared persistent luminescence, Acta. Mater. 155 (2018) 214-221.

[30] H. M .Li, J. Z. Cai, R. Pang, G. Y. Liu, S. Zhang, L. H. Jiang, D.Li, C. Y. Li, J. Feng, H. J. Zhang, J. A strategy for developing thermal-quenching-resistant emission and super-long persistent luminescence in $BaGa_2O_4:Bi^{3+}$, Mater. Chem. C. 2019, 7 (42) (2019) 13088-13096.

[31] H. M. Li, H. Y. Wu, R. Pang, G. Y. Liu, S. Zhang, L. H. Jiang, D. Li, C. Y. Li, J. Feng, H. J. Zhang, Investigation on the photoluminescence and thermoluminescence of $BaGa_2O_4:Bi^{3+}$ at extremely low temperatures, J. Mater. Chem. C. 9 (5) (2021) 1786-1793.

[32] V. Kahlenberg, R. X. Fischer, J. B. Parise, The stuffed framework structure of $BaGa_2O_4$, J. Solid. State. Chem. 154 (2) (2000) 612-618.

[33] L. L. Noto, D. Poelman, V. R. Orante-Barron, H. C. Swart, L. E. Mathevula, R. Nyenge, M. Chithambo, B. M. Mothudi, M. S. Dhlamini, Photoluminescence and thermoluminescence properties of $BaGa_2O_4$, Physica. B. 535 (2018) 268-271.

[34] X. Q. Zhou, G. F. Ju, T. S. Dai, Y. Li, H. Y. Wu, Y. H. Jin, Y. H. Hu, Strontium substitution enhancing a novel Sm^{3+}-doped barium gallate phosphor with bright and red long persistent luminescence, J. Lumin. 218 (2020) 8.

[35] H. Lin, D. L. Yang, G. S. Liu, T. C.Ma, B. Zhai, Q. D. An, J. Y. Yu, X. J. Wang, X. R. Liu, E. Y. B. Pun, Optical absorption and photoluminescence in Sm^{3+}- and Eu^{3+}-doped rare-earth borate glasses, J. Lumin. 2005, 113 (1-2) (2005) 121-128.

[36] J. X. Wang, Y. Xie, J. L. Guo, X. M. Yao, X. Geng, J. Gao, X. Y. Feng, Z. J. Zhou, Y. Y. Liu, B. Deng, R. J. Yu, Abnormal thermal quenching behavior and optical properties of a novel apatite-type $NaCa_3Bi(PO_4)_3F:Sm^{3+}$ orange-red-emitting phosphor for w-LED applications, Ceram. Int. 47 (20) (2021) 28167-28177.

[37] T. Wang, W. J. Bian, D. C. Zhou, J. B. Qiu, X. Yu, X. H. Xu, Red long lasting phosphorescence in $Ca_2Ge_7O_{16}:Sm^{3+}$ via persistent energy transfer from the host to Sm^{3+}, Mater. Res. Bull. 74 (2016) 151-155.

[38] M. H. Wu, S. Y. Liu, Y. C. Sun, W. Chen, L. F. Huang, G. L. Chen, Z. S. Zheng, Energy transfer of wide band long persistent phosphors of Sm^{3+}-Doped $ZrSiO_4$, Mater. Chem. Phys. 251 (2020) 123086.

[39] K. Van den Eeckhout, P. F. Smet, D. Poelman, Persistent luminescence in Eu^{2+}-doped compounds: A Review. Materials. 3 (2010) 2536.

[40] J. Xu, S. Tanabe, Persistent luminescence instead of phosphorescence: History, mechanism, and perspective, J. Luimn. 205 (2019) 581-620.

[41] J. Q. Xiahou, Q. Zhu, L. Zhu, S. Huang, T. Zhang, X. D, Sun, J. G. Li, Lattice-site engineering in $ZnGa_2O_4:Cr^{3+}$ through Li^+ doping for dynamic luminescence and advanced optical anti-counterfeiting, J. Mater. Chem. C. 10 (2022) 7935-7948.

[42] T. Si, Q. Zhu, T. Zhang, X. D. Sun, J. G. Li, Co-doping Mn^{2+}/Cr^{3+} in $ZnGa_2O_4$ to fabricate chameleon-like phosphors for multi-mode dynamic anti-counterfeiting, Chem. Eng. J. 426 (2021) 131744.

[43] H. Suo, C. Guo, Z. Yang, S. Zhou, C. Duan, M. Yin, Thermometric and optical heating bi-functional properties of upconversion phosphor $Ba_5Gd_8Zn_4O_{21}:Yb^{3+}/Tm^{3+}$, J. Mater. Chem. C. 3 (28) (2015) 7379-7385.

[44] Hai, M. K. Pei, Q. Ren, X. L. Wu, E. L. Yang, D. Xu, J. F. Zhu, Ag nanoparticles significantly improve the slow decay brightness of $SrAl_2O_4:Eu^{2+}$, Dy^{3+} by the surface plasmon effect, Dalton. T. 51 (6) (2022) 2287-2295.

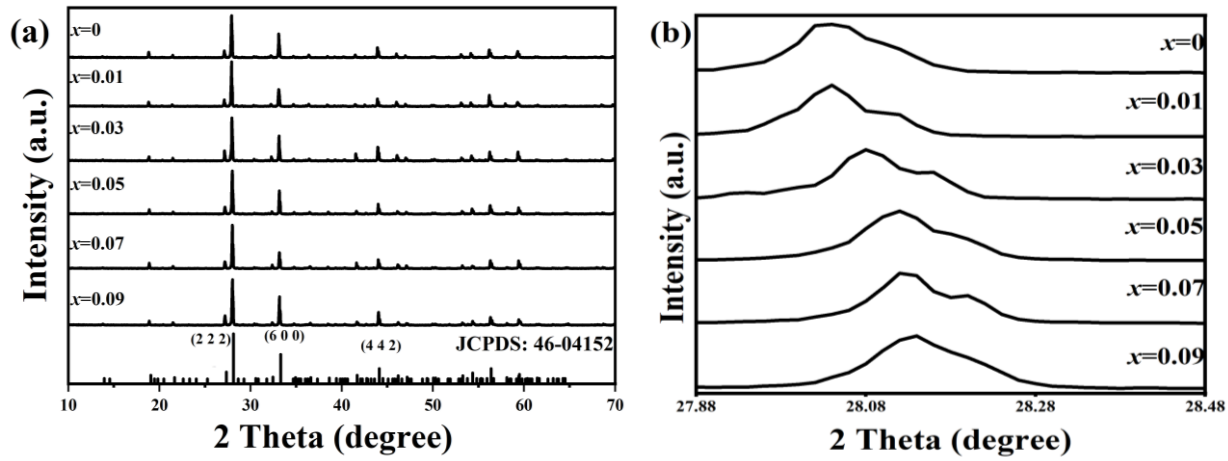

Fig. 1. (a) X-ray diffraction patterns and (b) enlarged (222) diffraction of BGSO:Sm^{3+} (x = 0- 0.09).

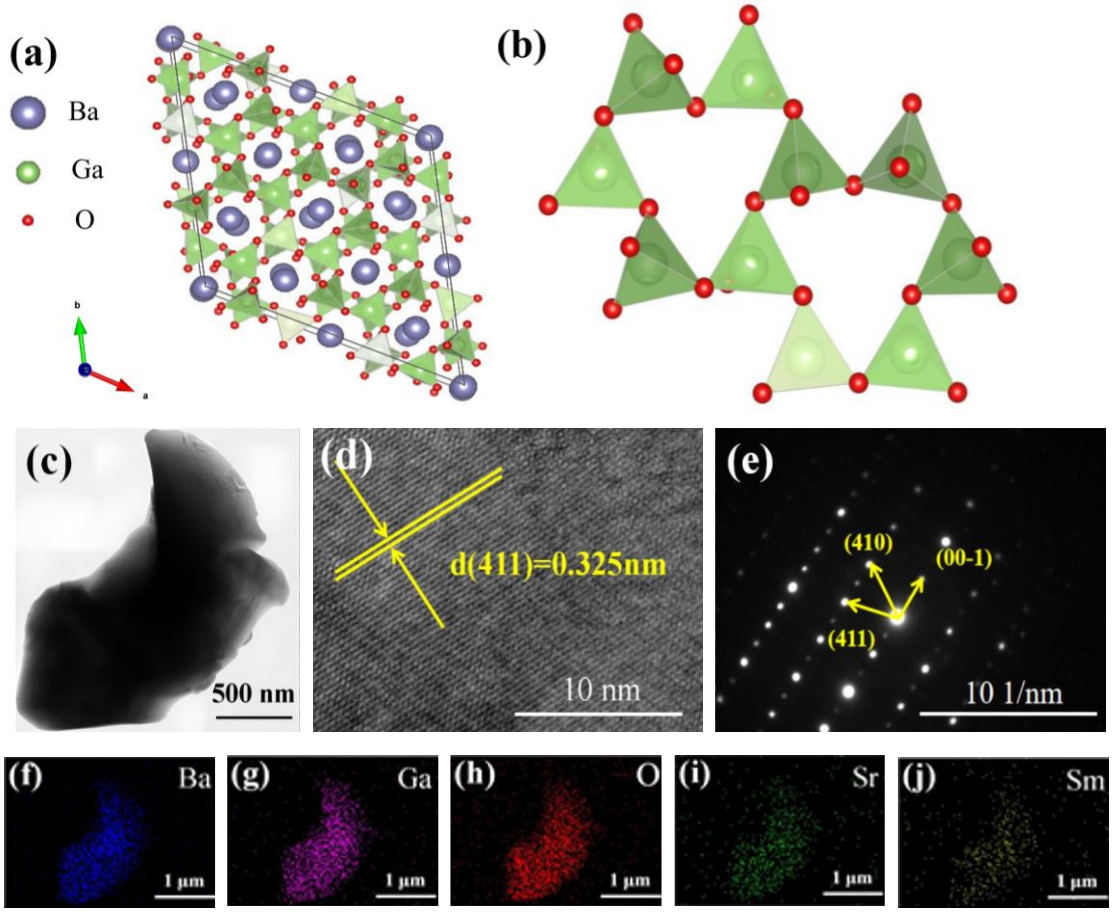

Fig. 2. (a) Crystal unit cell of $BaGa_2O_4$ viewed along the c-axis, (b) two different types of six-membered rings consisted of Ga-O tetrahedron, (c) TEM image, (d) HR-TEM image, (e) SAED pattern, and (f-j) element distribution of BGSO:Sm^{3+} (x = 0.07).

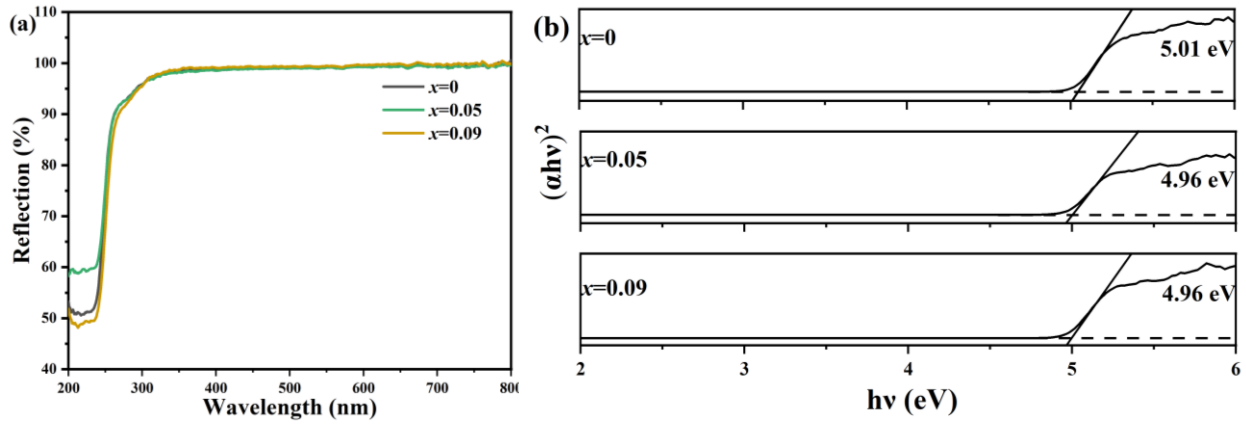

Fig. 3. (a) Diffuses reflection spectra and (b) the bandgap energies of the BGSO (x = 0, 0.05, 0.09).

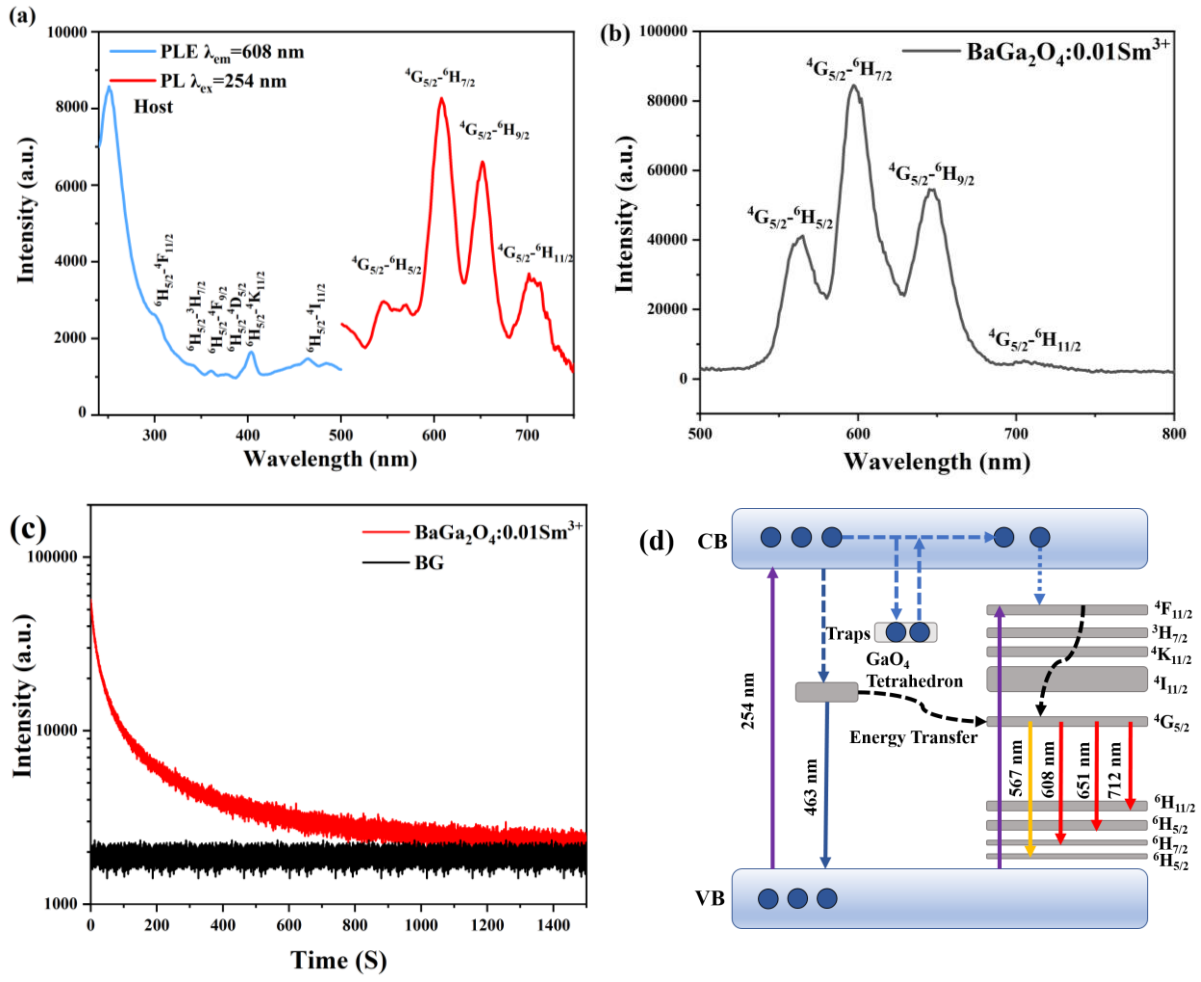

Fig. 4. (a) PLE and PL spectra, (b) persistent luminescence spectra, (c) persistent luminescence decay curve of $BaGa_2O_4$:0.01Sm^{3+}, and (d) schematic illustration of the luminescence mechanism for $BaGa_2O_4$:0.01Sm^{3+}.

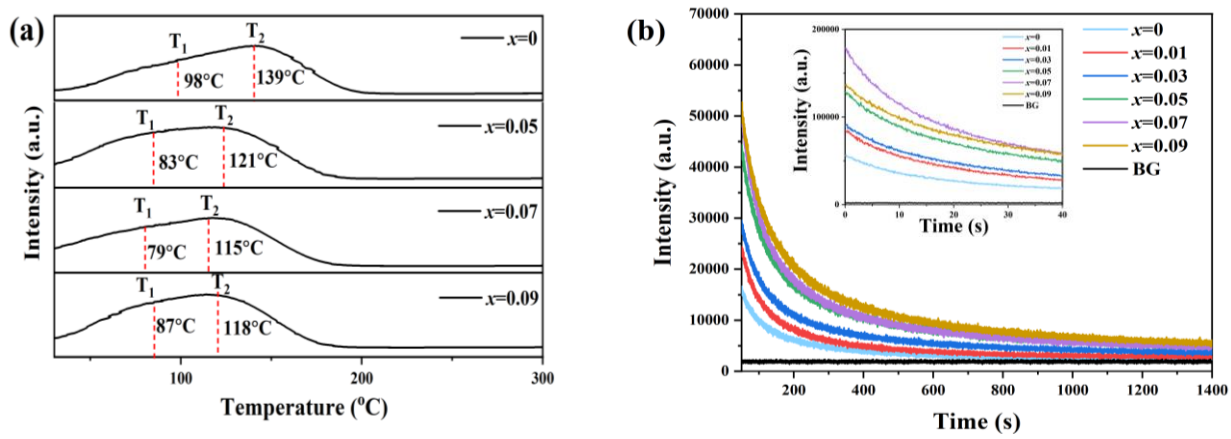

Fig. 5. (a) TL glow curves for BGSO:Sm^{3+} (x = 0, 0.05, 0.07, 0.09) and (b) the persistent luminescence decay curves (monitored at 608 nm after 254-nm UV light illumination for 5 min).

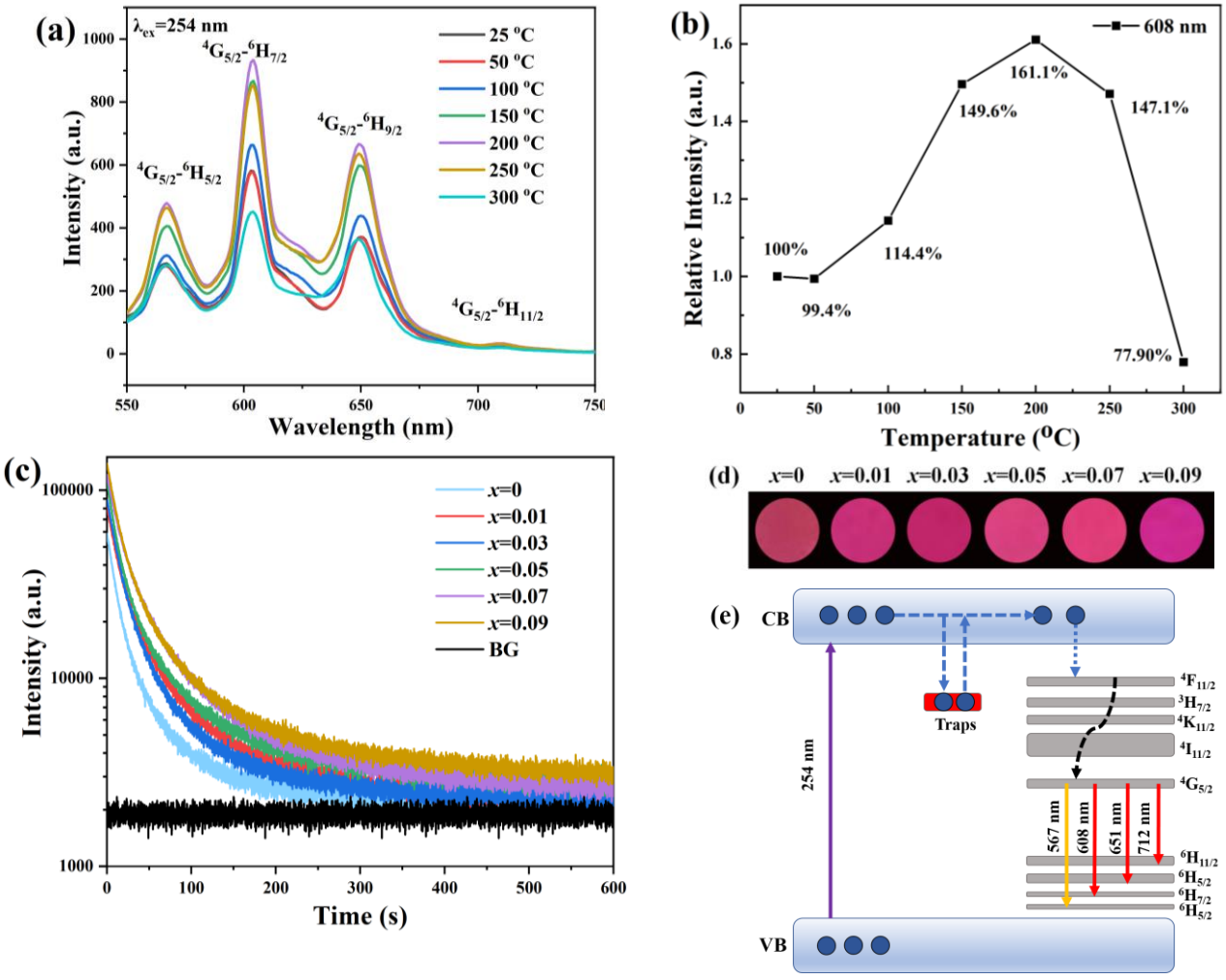

Fig. 6. (a) PL spectra of BGSO:Sm^{3+} (x = 0.07) at different temperatures, (b) the relative intensities of 608 nm at different temperatures for BGSO:Sm^{3+} (x = 0.07), (c) persistent luminescence decay curves of BGSO:Sm^{3+} (x = 0-0.09) after heating at 150 ^{o}C, (d) appearances of BGSO:Sm^{3+} (x = 0.07) phosphors at different temperatures

under 254 nm light excitation, and (e) schematic illustration of the luminescence mechanism for BGSO:Sm^{3+} after heat processing.

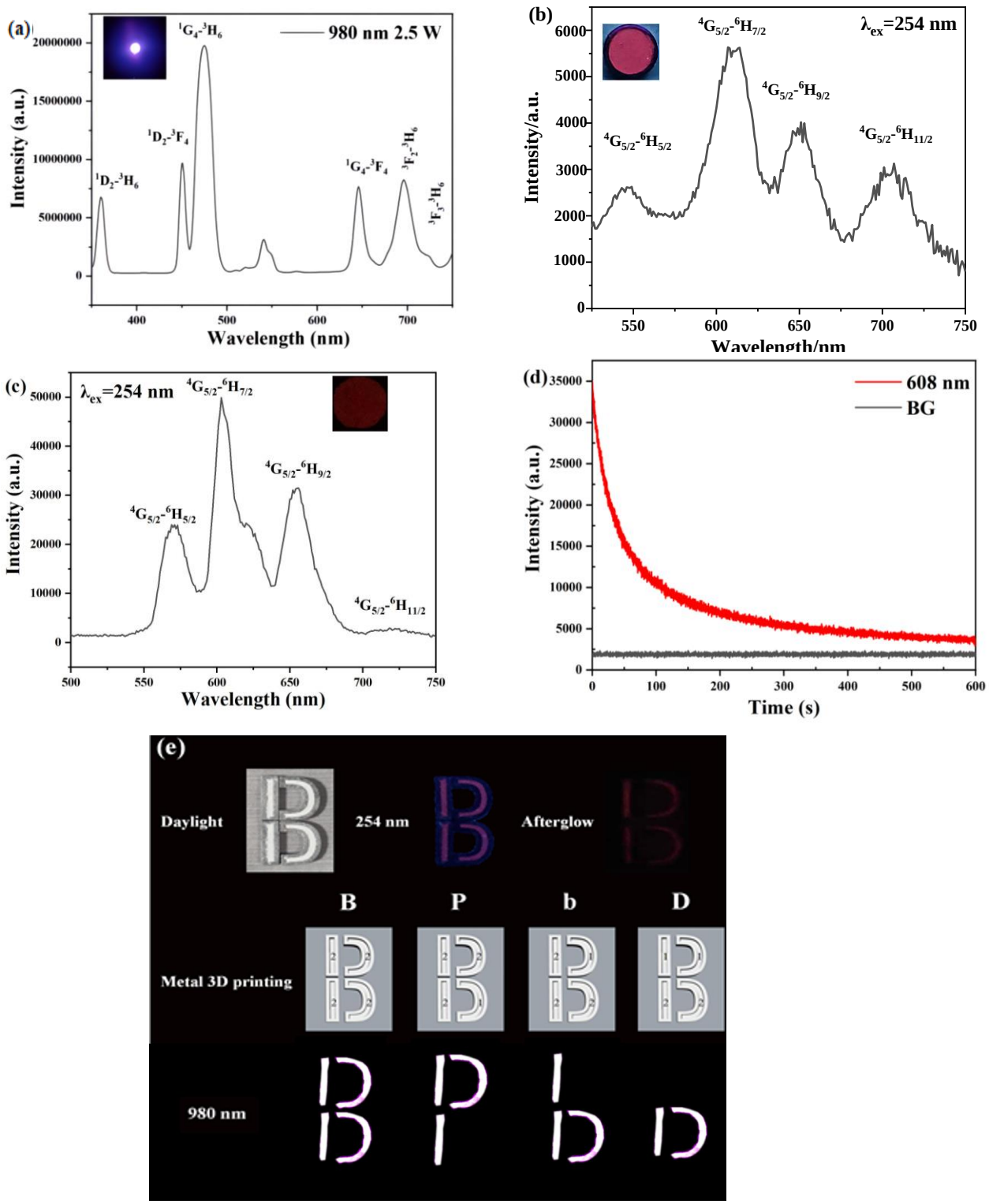

Fig. 7. PL spectra and the appearance of the mixture phosphor (a) under 980 nm laser excitation (2.5 W) and (b) under 254-nm UV light excitation, respectively. (c) and (d) are the persistent luminescence spectra and the afterglow and the persistent

luminescence decay curves of the mixture phosphor. The mixture phosphor is composed of $Ba_{0.93}Sr_{0.07}Ga_2O_4$:0.01$Sm^{3+}$ and $NaYF_4$:Yb^{3+},Tm^{3+} with the weight ratio of 1:1. (e) is the designed logo for anti-counterfeiting application, with phosphor 1 as $Ba_{0.93}Sr_{0.07}Ga_2O_4$:0.01$Sm^{3+}$ and phosphor 2 as the mixture phosphor.

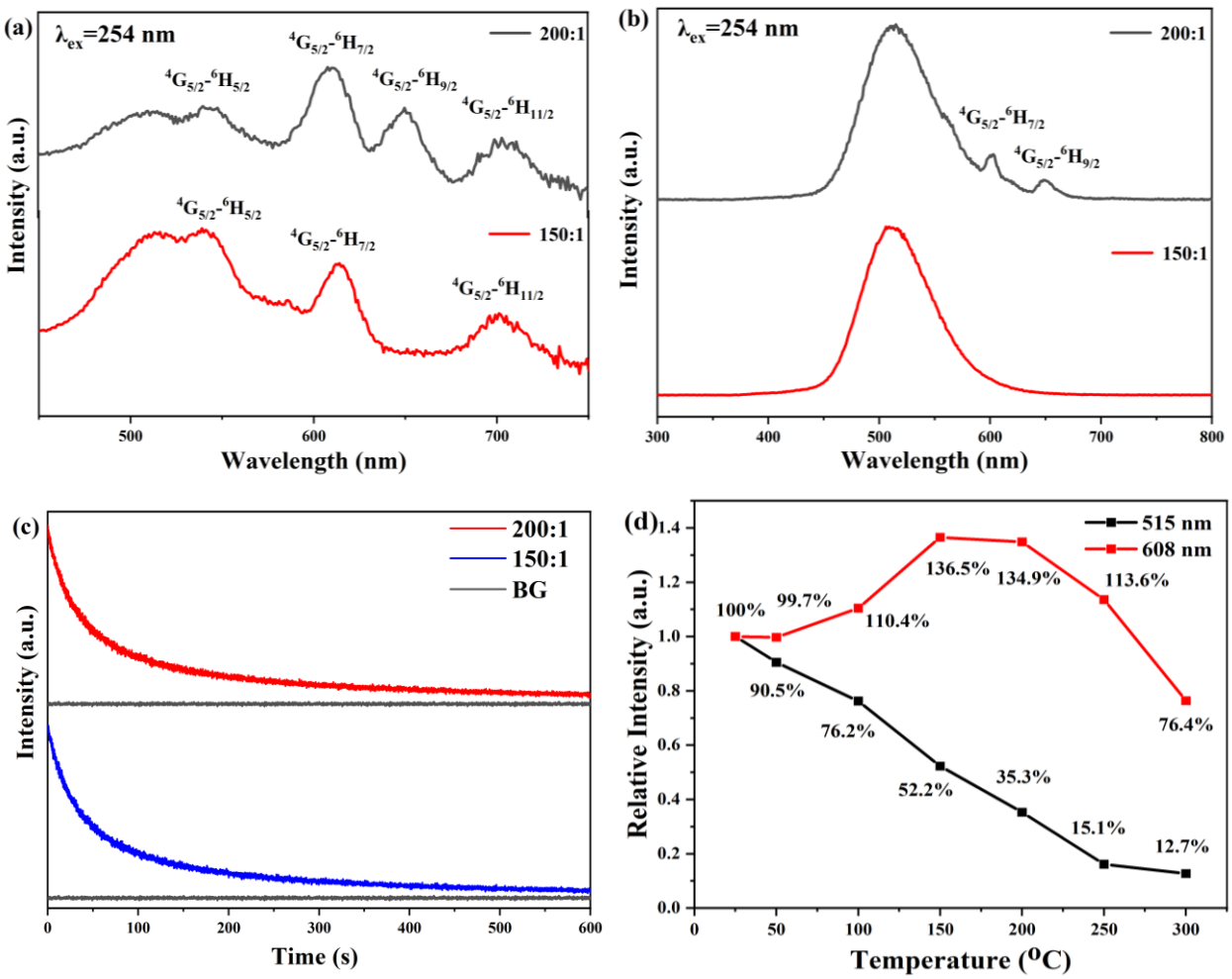

Fig. 8. (a) PL spectra, (b) the persistent luminescence spectra, and (c) persistent luminescence decay curves of two typical mixture phosphors, with the weight ratio of $Ba_{0.93}Sr_{0.07}Ga_2O_4$:0.01$Sm^{3+}$ to $SrAl_2O_4$:Eu^{3+}, Dy^{3+} as 200:1 and 150:1, respectively. (d) is the relative intensities of 515 nm and 608 nm at different temperatures for the mixtures, with the weight ratio of $Ba_{0.93}Sr_{0.07}Ga_2O_4$:0.01$Sm^{3+}$ to $SrAl_2O_4$:Eu^{3+}, Dy^{3+} as 150:1.

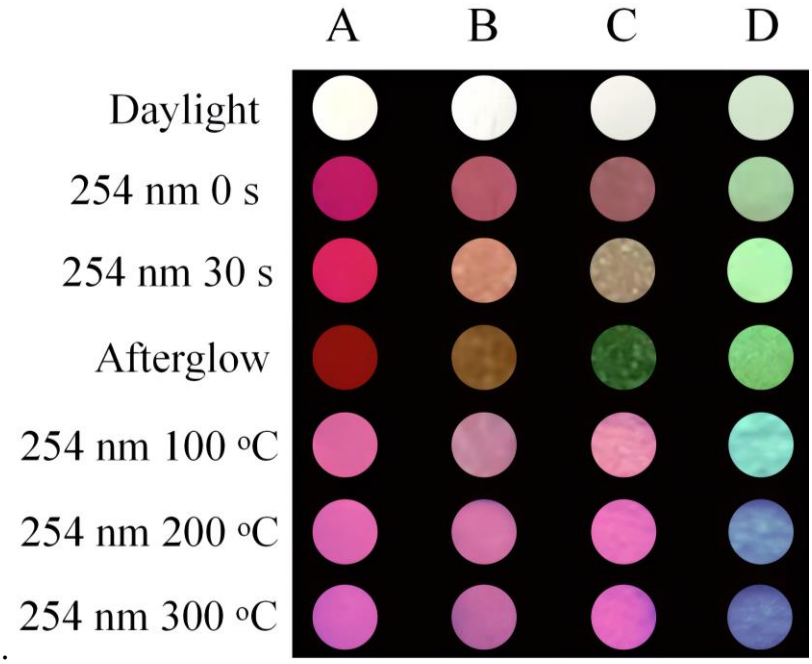

Fig. 9. Appearances of four typical samples under daylight, 254 nm UV light for 0s and 30 s at different temperatures, and the afterglows after removing the UV light source. Sample A is $Ba_{0.93}Sr_{0.07}Ga_2O_4$:0.01$Sm^{3+}$ and sample D is the mixture of $BaSO_4$ and $SrAl_2O_4$:Eu^{3+}, Dy^{3+} (the weight ratio is 100:1). The weight ratio of $Ba_{0.93}Sr_{0.07}Ga_2O_4$:0.01$Sm^{3+}$ to $SrAl_2O_4$:Eu^{3+}, Dy^{3+} is 200:1, 150:1 for samples B and C respectively.

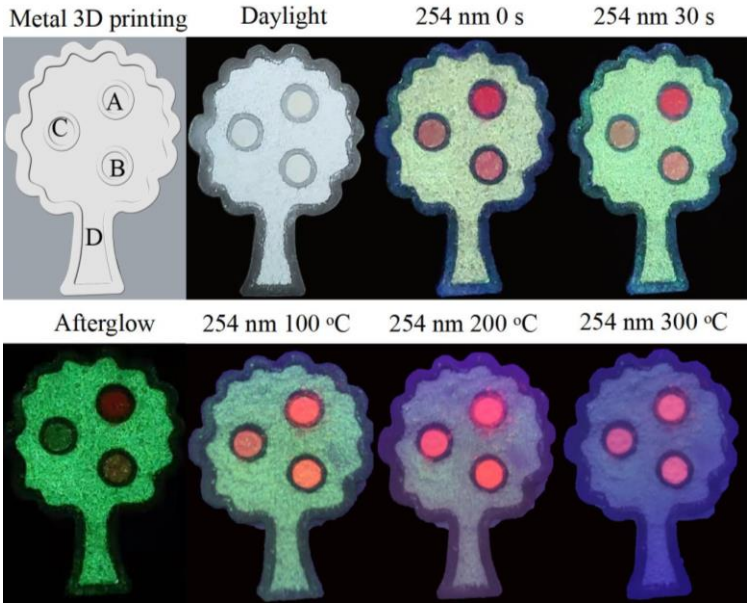

Fig. 10. Appearances of the signals for the pattern of "apple tree" with four typical samples placed in the designed container fabricated by metal 3D printing.

Supporting Information

A building-block strategy for dynamic anti-counterfeiting by using $(Ba,Sr)Ga_2O_4:Sm^{3+}$ new red persistent luminescent phosphor as an important component

Ao Guo[a], Qi Zhu[a,*], Shimeng Zhang[a], Xudong Sun[b] and Ji-Guang Li[c,*]

[a]*Key Laboratory for Anisotropy and Texture of Materials (Ministry of Education), School of Materials Science and Engineering, Northeastern University, Shenyang, Liaoning 110819, China*

[b]*Foshan Graduate School of Northeastern University, Foshan, Guangdong 528311, PR China*

[c]*Research Center for Functional Materials, National Institute for Materials Science, Namiki 1-1, Tsukuba, Ibaraki 305-0044, Japan*

*E-mail: zhuq@smm.neu.edu.cn and LI Jiguang@nims.go.jp

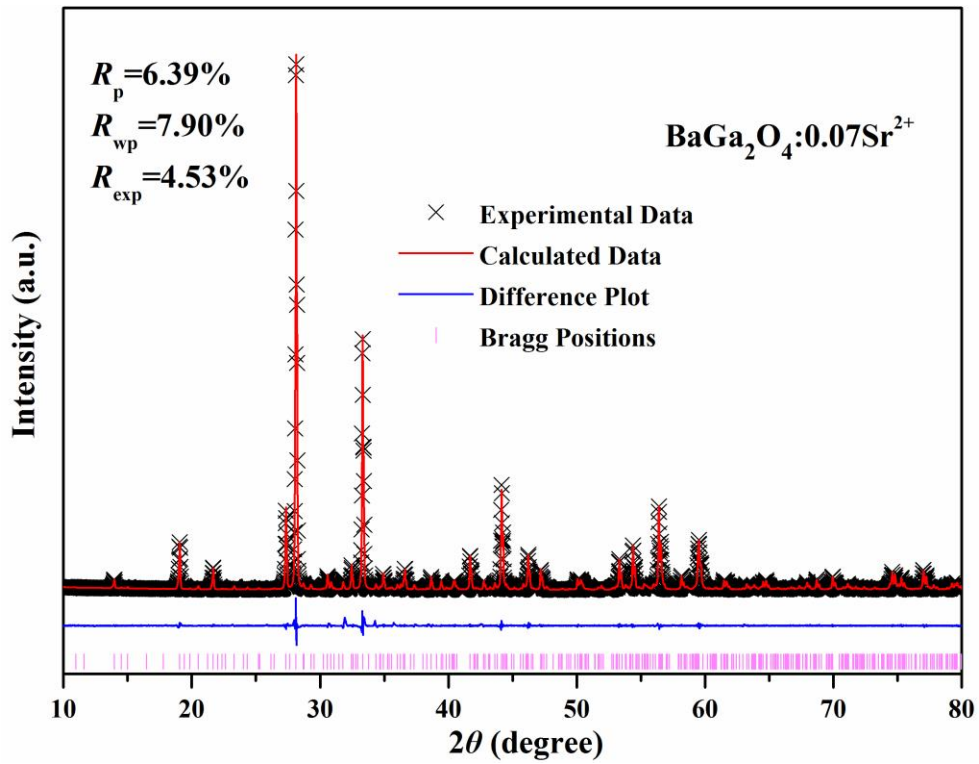

Figure S1. Rietveld refinements of BGSO (x=0.07 sample).

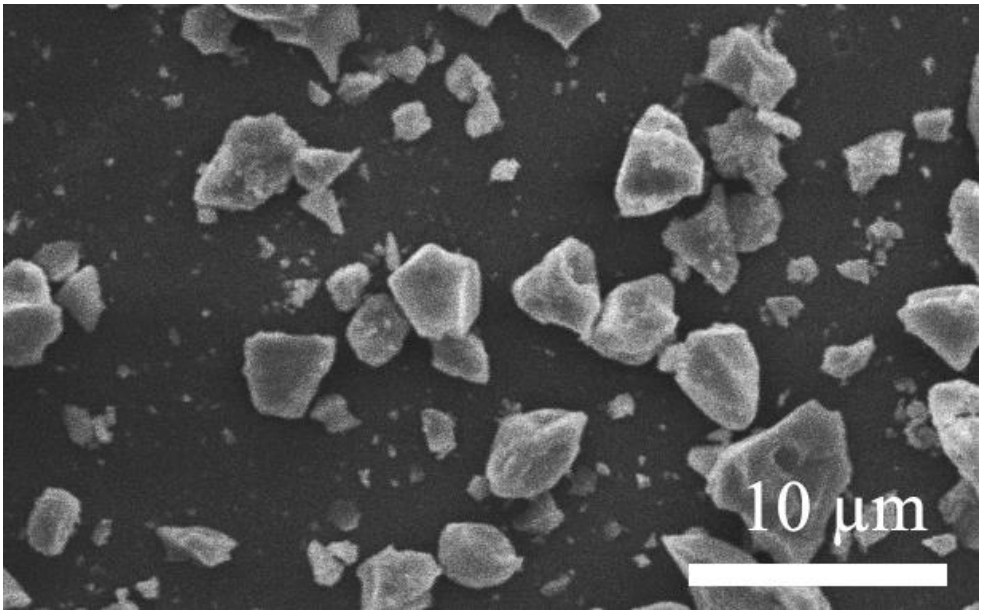

Figure S2. FE-SEM image of BGSO:Sm^{3+} (x = 0.07) powder.

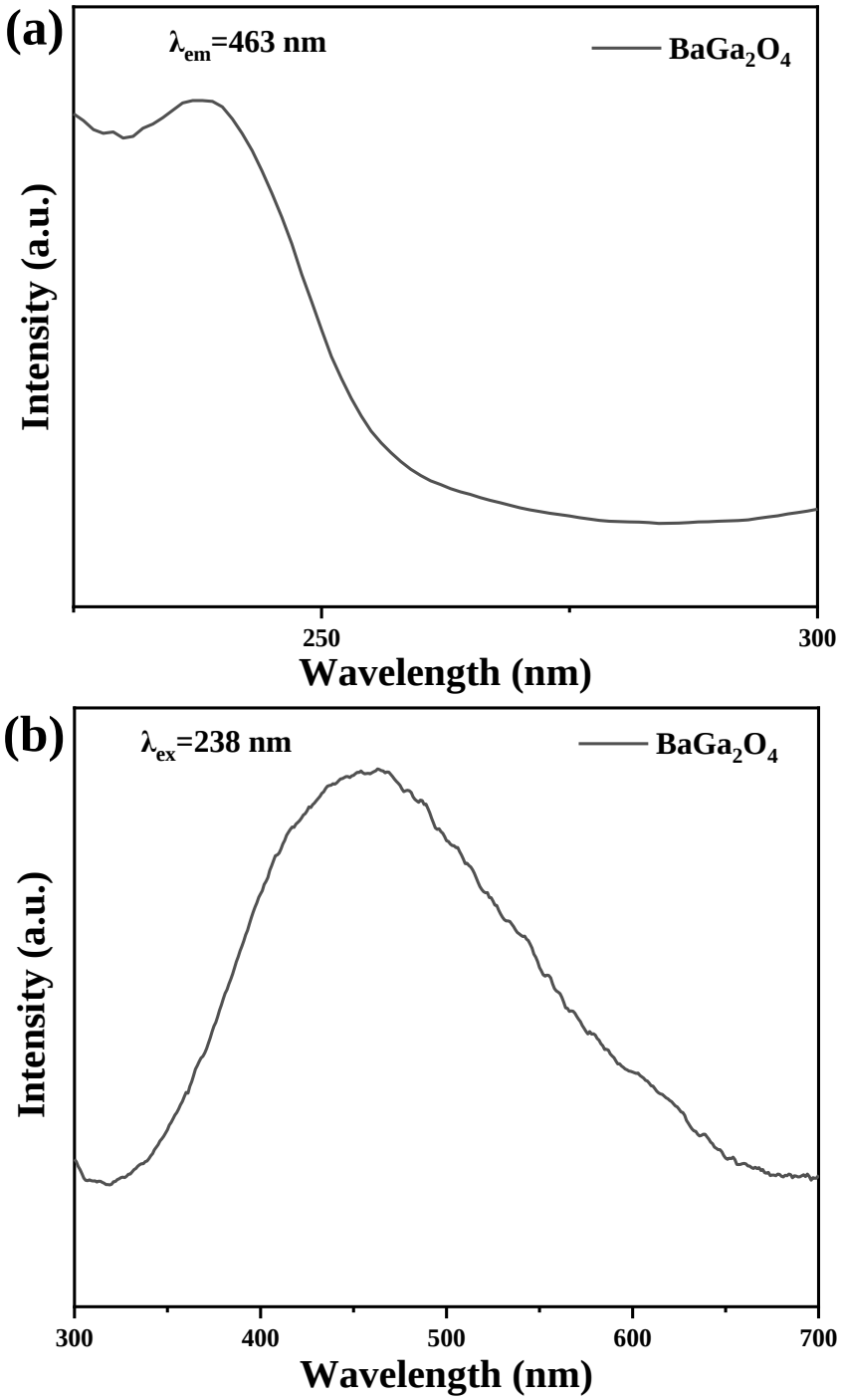

Figure S3. (a) PLE spectra and (b) PL spectra of $BaGa_2O_4$.

A building-block strategy for dynamic anti-counterfeiting by using (Ba,Sr)Ga_2O_4:Sm^{3+} new red persistent luminescent phosphor as an important component

Ao Guo[a], Qi Zhu[a,*], Shimeng Zhang[a], Xudong Sun[b] and Ji-Guang Li[c,*]

[a]*Key Laboratory for Anisotropy and Texture of Materials (Ministry of Education), School of Materials Science and Engineering, Northeastern University, Shenyang, Liaoning 110819, China*

[b]*Foshan Graduate School of Northeastern University, Foshan, Guangdong 528311, PR China*

[c]*Research Center for Functional Materials, National Institute for Materials Science, Namiki 1-1, Tsukuba, Ibaraki 305-0044, Japan*

*Corresponding author

Dr. Qi Zhu

Tel: +86-24-8367-2700

E-mail: zhuq@smm.neu.edu.cn

Dr. Ji-Guang Li

Tel: +81-29-860-4394

E-mail: LI.Jiguang@nims.go.jp

Abstract

Long persistent luminescence materials developed to commercial standards are primarily concentrated in the blue and green regions, with only a few in the red region. Red, as one of the three basic colors, can be mixed in various proportions with blue and green to yield various colors. The development of red persistent phosphors has a broader application potential but remains a challenge. A solid-state reaction method was used to synthesize new red persistent luminescent materials of $Ba_{1-x}Sr_xGa_2O_4:Sm^{3+}$ (x = 0–0.09). In $BaGa_2O_4$, both Sr^{2+} and Sm^{3+} preferentially occupy the Ba^{2+} site rather than the Ga^{3+} site. When exposed to UV light at 254 nm, the phosphors emit the characteristic red emission of Sm^{3+} at wavelengths ranging from 500 nm to 750 nm. After removing the UV light source, an intense red afterglow that lasted more than 1400 seconds was observed. The red afterglow signal reappears after a heating process. Doping Sr^{2+} reduces the trap depth and improves the red persistent luminescence significantly. Because the escaped electrons from traps compensate for the emission loss of Sm^{3+} during the heating process, the red phosphors have unimaginably luminescent thermal stability. Thus, the emission intensity at 200 °C is 1.6 times that at room temperature. The prepared red persistent phosphors show multimode luminescence, with the output signal being time and temperature sensitive, indicating that they are potential luminescent materials for anti-counterfeiting applications. Finally, a building-block strategy for advanced anti-counterfeiting applications of dynamic display information is proposed, with red persistent phosphors serving as an important component combined with upconversion phosphors of $NaYF_4:Yb^{3+}$, Tm^{3+}, and green persistent phosphors of $SrAl_2O_4:Eu^{2+}$, Dy^{3+}.

Keywords:

Long persistent luminescence; Temperature-dependent luminescence; Anti-counterfeiting; $BaGa_2O_4$; Sm^{3+}

1. Introduction

There are some luminescent materials, that can continue to emit light for a certain period of time even after the external light source excitation is eliminated [1,2]. These materials are known as long persistent luminescence materials, and they are commonly used in places that require low lightings, such as night lights, traffic signs, and indoor safety escape signs [3,4]. They have recently been employed in radiation detection and optical storage media after adequate research and development [5,6]. Long persistent luminescent materials have been used in anti-counterfeiting, in vivo imaging, and medical diagnosis [7-10]. At the moment, materials with green and blue afterglow, such as $SrAl_2O_4:Eu^{2+}$, Dy^{3+} (green), and $CaAl_2O_4:Eu^{2+}$, Nd^{3+} (blue), have reached commercial standards, whereas red long persistent luminescence materials are difficult to attain these standards in terms of afterglow time and brightness [11,12]. Because red is one of the three basic colors, it can be mixed in various proportions with blue and green to produce various colors, giving it a broader application prospect [13-16]. Therefore, it is critical to developing red long persistent luminescence materials with superior properties.

Typically, emitting centers are critical for materials with persistent luminescence. The emitting color is always determined by the doped ions and the host materials. The host is fixed, but the doped ions can be changed. In other words, the afterglow color of the synthesized afterglow materials will be affected by the choice of different doped ions. When excited under certain conditions, Eu^{2+}, Eu^{3+}, Mn^{2+}, Sm^{3+}, or Pr^{3+} can produce red light [17-21]. Furthermore, through energy transfer processing [22], the emitting color of persistent luminescence materials can be changed because energy transfer from one ion to another doped ion during afterglow decay contributes to another afterglow, including red afterglow. This type of red long persistent luminescence was discovered in $Sr_3MgSi_2O_{8-1.5x}N_x:Eu^{2+},Dy^{3+},Mn^{2+}$, and $BaMg_2Si_2O_7:Eu^{2+},Dy^{3+},Mn^{2+}$ [23,24]. However, the duration and brightness of the afterglow are short and dim. Red long persistent luminescence materials such as $Ca_2SnO_4:Sm^{3+}$, $Y_2O_2S:Sm^{3+}$, and $Sr_2SnO_4:Sm^{3+}$ have been studied recently [25-27].

The typical transition between Sm^{3+} electronic configurations has been reported to contribute to a strong red emission [28]. As a result, Sm^{3+} is always used in red phosphors and red long persistent luminescence materials.

In addition to being influenced by doped ions, the intensity and duration of the persistent afterglow are determined by phosphor traps [29]. When the excitation is stopped, the trapped electrons or holes will be released to the emitting centers via the conduction or valence bands. It is believed that the traps are related to defects. Li et al. discovered a novel red-orange-emitting phosphor, $BaGa_2O_4:Bi^{3+}$, with $BaGa_2O_4$ as the host [30]. Because of the efficient traps formed by defects during the formation of $BaGa_2O_4$, $BaGa_2O_4:Bi^{3+}$ exhibited a long afterglow at extremely low temperatures [31]. Furthermore, this phosphor has excellent thermal stability, as its integrated intensity at 200 ˚C retains more than 88.1% of that at room temperature. As a result, this persistent luminescence material has promising applications in both extremely low and high-temperature conditions. As a result, $BaGa_2O_4$ could be used as a suitable host for long persistent luminescence phosphors.

Except for the host, the defects can be formed by doped ions occupying the site of host matrix ions with a different valence or ionic radius. A solid-state reaction method was used to synthesize $Ba_{1-x}Sr_xGa_2O_4:0.01Sm^{3+}$ (x = 0–0.09), a group of red persistent phosphors, with smaller Sr^{2+} substituting the larger Ba^{2+} to improve the persistent luminescence of $BaGa_2O_4:Sm^{3+}$. The samples were then characterized using XRD, UV-Vis, HRTEM, SAED, TL, PLE/PL spectroscopy, and persistent luminescence decay analysis. Finally, the possibility of their use in anti-counterfeiting applications was investigated.

2. Experimental section

2.1. Sample preparation

$Ba_{1-x}Sr_xGa_2O_4:0.01Sm^{3+}$ (x = 0, 0.01, 0.03, 0.05, 0.07, 0.09) samples, which are described as BGSO:Sm^{3+}, were synthesized by the high-temperature solid-state reaction method. $BaCO_3$, Ga_2O_3, Sm_2O_3, and $SrCO_3$ were chosen as the raw materials,

all purchased from Sinopharm (Shanghai, China) with a purity of 99.9%. Based on the stoichiometric ratio after calculation, all the raw materials were weighted by the electronic balance. The powders were ground for 30 min and then the mixture was calcined at 1400 ^{o}C for 8 hours. When cooling to room temperature, the powders were tested after ground again.

2.2. Characterization

The powder X-ray diffraction patterns were collected by X-ray diffraction (XRD, Model SmartLab, Rigaku, Tokyo, Japan) at the scanning rate of 8 min^{-1} in the 2θ range from 10^{o} to 70^{o}, operating at 40 mA and 40 kV using monochromated Cu Kα as radiation. The photoluminescence spectra (PL)/photoluminescence excitation spectra (PLE) of samples were obtained by the FP-8600 (JASCO, Tokyo) with a 150 W Xe-lamp as the excitation source. The diffuse reflectance spectra of the samples were acquired by a UV-vis spectrophotometer (UV-3600 Plus, Shimadzu, Kyoto, Japan). Long persistent luminescence spectra were recorded *via* the Horiba JY Fluorolog-3 (Kyoto) spectrofluorometer. An FJ-427A TL spectrofluorometer (Beijing Nuclear Instrument Factory, Beijing, China) at a heating rate of 1 K s^{-1} was used to gain Thermoluminescence (TL) curves after the samples were excited for 5 min by a UV lamp. In order to study the application in anti-counterfeiting, the commercial persistent phosphor of $SrAl_2O_4:Eu^{3+}$, Dy^{3+} (Luming Science and Technology Group Co., Ltd, China) was chosen here as a green light source. The afterglow luminance of sample was measured by a spectroradiometer (HS-1000, Photal Otsuka Electronics, Osaka, Japan) with a built-in software of the system.

3. Results and discussion

3.1. Synthesis and crystal structure

Fig. 1a depicts the XRD patterns of BGSO:Sm^{3+} (x = 0–0.09). All the XRD diffraction peaks are consistent with the standard patterns of $BaGa_2O_4$ (JCPDS NO. 46-0415), indicating the formation of a single phase of BGSO:Sm^{3+}. Because the ionic radii of Sm^{3+} (1.02 Å, CN = 7; 0.958 Å, CN = 6) and Sr^{2+} (1.21 Å, CN = 7; 1.18

Å, CN = 6) are close to that of Ba^{2+} (1.38 Å, CN = 7) and much larger than that of Ga^{3+} (0.47 Å, CN = 4), Sm^{3+} and Sr^{2+} ions are thought to substitute for Ba^{2+} sites. Furthermore, because the ionic radius of Sm^{3+} and Sr^{2+} is smaller than that of Ba^{2+}, the incorporation of Sm^{3+} and Sr^{2+} causes the shrink of lattice. The enlarged drawing of the (222) main diffraction peaks is show in Fig.1b. As the *x* value increases from 0 to 0.09, the (222) diffraction peak shifts to the higher angle side. This is primarily due to that smaller Sr^{2+} ions substitute the larger Ba^{2+} ions, causing the lattice to shrink. To test this inference, the Rietveld refinement results of the XRD pattern for BGSO (*x* = 0.07 sample) are analyzed and shown in Figure S1. The calculated results agree with the experimental data. The R_{wp}, R_p, and R_{exp} values are quite low, indicating that the results reliable. Interstitial oxygen is generated when Ba^{2+} ions are replaced by Sm^{3+} ions to compensate for the charge difference. This could contribute to long persistent luminescence.

The unit cell structure of $BaGa_2O_4$ is depicted in Fig. 2a. The hexagonal structure of $BaGa_2O_4$ belongs to the $P6_3$ space group. $BaGa_2O_4$ comprises six-membered ring layers of GaO_4 tetrahedra that are perpendicular to the *c*-axis, with its layers stacked to form a three-dimensional framework. Tunnels are formed by the superposition of the layers parallel to the *c*-axis, and the barium cations are in these tunnels. There are two types of barium ions: one with nine oxygen atoms located in a more symmetrical Ga-O tetrahedron six-membered ring, and the other with seven and eight oxygen atoms located in a more irregular Ga-O tetrahedron six-membered ring (Fig. 2b) [32]. Figures S2 and 2c show the FE-SEM and TEM morphology of BGSO:Sm^{3+} (*x* = 0.07) sample, indicating a particle size of 1–5 μm. The HRTEM image (Fig. 2c) and SAED patterns were examined (Fig. 2d). The HRTEM image's clear lattice fringes indicate that the sample has good crystallinity. The distance between the two crystal planes is about 0.325 nm. As a result, they correspond to the (411) crystallographic plane (d(411) = 0.32612 nm, JCPDS No. 46-0415). The calculated values of the diffraction spots, as shown in Fig. 2d, are approximately 0.325 nm, 0.352 nm, and 0.432 nm, which correspond to the (411), (410), and (00-1) planes, respectively (d(410) =

0.35216 nm, d(00-1) = 0.43326 nm, JCPDS No. 46-0415). The elemental distribution results in Fig. 2e-g show that Sr^{2+} and Sm^{3+} are successfully doped and that the chemical elements are homogeneously distributed.

3.2. Photoluminescence properties

Fig. 3a depicts the diffuse reflectance spectra of the BGSO (x = 0, 0.05, and 0.09) samples. The peak from 200 nm to 300 nm is attributed to the absorption of $BaGa_2O_4$ host [33]. The substitution of Sr^{2+} ions for Ba^{2+} sites did not affect the absorption. The Kubelka-Munk formula was used to calculate the band gap energy of the hosts [34]:

$$F(R) = \frac{(1-R)^2}{2R}$$

$$(\alpha h\nu)^2 = A(h\nu - E_g)$$

where R denotes the reflectivity of the sample, α denotes the absorption coefficient, which is proportional to $F(R)$, h denotes Planck's constant, ν denotes the light frequency, and A denotes the proportionality constant. The intercept of the diffuse reflection spectra transformed by the Kubelka-Munk function F(R) in Fig.3b can be used to calculate the bandgap energy. The bandgap of $BaGa_2O_4$ is approximately 5.01 eV. The band gap shrinks slightly as the Sr^{2+} doping content increase because the determined values are around 4.96 eV for x = 0.05 and x = 0.09 samples, which are smaller than 5.01 eV.

The PLE and PL spectra of $BaGa_2O_4$:0.01Sm^{3+} are shown in Fig.4a. The $O^{2-} \rightarrow Ga^{3+}$ charge transfer band is assigned to the strong band at 254 nm in the PLE spectra [33]. Because the host absorption of $BaGa_2O_4$ is close to the charge transfer band, the strong band could overlap the charge transfer band and the host absorption band. Sharp peaks ranging from 300 nm to 450 nm correspond to the Sm^{3+} intra-$4f^5$ transitions, with the $^6H_{5/2} \rightarrow {}^4K_{11/2}$ transition at 404 nm dominating [28]. The PL spectra obtained at an excitation wavelength of 254 nm show four narrow emission bands attributed to the $^4G_{5/2}$ to the $^6H_{5/2}$ (568 nm), $^6H_{7/2}$ (608 nm), $^6H_{9/2}$ (651 nm), and $^6H_{11/2}$ (707 nm) transitions of Sm^{3+}, with the sharp peak at 608 nm dominating [35,36].

The persistent luminescence spectra of $BaGa_2O_4$:0.01Sm^{3+} at room temperature are shown in Fig. 4b, which are nearly identical to the emission spectra of Sm^{3+}. When the sample is excited by a 254 nm UV light, four emission bands are observed at 568 nm, 608 nm, 651 nm, and 707 nm. Fig. 4c depicts the decay curve of persistent luminescence. A UV lamp was used to excite the sample for 5 min at room temperature. The red afterglow of the samples lasts more than 1400 seconds. The schematic energy level diagrams of $BaGa_2O_4$:0.01Sm^{3+} in Fig. 4d show the possible luminescence mechanism. The ground-state electrons of Sm^{3+} ions are promoted to the conduction band by UV irradiation. The excited states of Sm^{3+} are degenerated with free electron-hole states, with an electron at the bottom of the conduction band and a hole at the top of the valence band, because of the UV light excitation. Some excited electrons are delocalized in the CB and are captured by the GaO_4 tetrahedron. The electrons released from the GaO_4 tetrahedron to VB contribute to the blue emission [37], as evidenced by the host emission (Figure S3). Simultaneously, some electrons are relaxed to the excited levels of Sm^{3+} and relaxed to the $^4G_{5/2}$ level, and the energy relaxes through the transitions from $^4G_{5/2}$ to the $^6H_{5/2}$, $^6H_{7/2}$, $^6H_{9/2}$, and $^6H_{11/2}$ levels, contributing to the emission at 568, 608, 651, and 707 nm. Furthermore, the possible energy transfer from the GaO_4 tetrahedron to the $^4G_{5/2}$ energy level contributes to Sm^{3+} emission. When electrons are excited from the valence band to the conduction band by UV excitation, some electrons are captured and retained by the electron trap. During the illumination period, the electron traps are filled. When the ultraviolet irradiation excitation stops, the trapped electrons escape to the conduction band and then to the excited energy levels of Sm^{3+}, contributing to the afterglows [37, 38].

Electronic traps are critical for all long persistent luminescence materials. Shallow traps require less energy to allow captured electrons to escape more easily, comparing to deep traps. We used thermoluminescence (TL) to determine the trap depth of the samples. The TL glow curves for the samples as shown in Fig. 5a. The TL curves are not symmetrical, and there are two peaks in the TL curves corresponding to the shallow and deep traps, respectively. These two peaks are caused

by two different defects: charge compensation defects caused by Sm^{3+} replacing Ba^{2+} and the lattice distortion defects formed by the substitution of Sm^{3+} and Sr^{2+} for Ba^{2+}.

The trap depth can be calculated by the following equation [39]:

$$E = \frac{T_m}{500}$$

where T_m denotes the temperature for which the glow curve reaches a maximum, and E denotes the approximate trap depth. The trap depth for each sample is summarized in Table 1. The peaks of T_1 and T_2 shift to the lower temperature side as the x value increases, indicating that Sr^{2+} doping makes the traps shallower on the overall trend. Fig. 5b depicts the decay curves of persistent luminescence. A UV lamp was used to excite all the samples for 5 min at room temperature. The red afterglow in all samples lasts longer than 1400 seconds, because the afterglow luminance at 1400 s is estimated to be ~0.7–1.1 mcd/m^2, which is greater than the value of 0.32 mcd/m^2 [40]. Obviously, there are two types of laws for the decay curves at the initial and later parts. Increasing the x value from 0 to 0.07 results in a more intense afterglow for the initial duration (before 35 s), but increasing the x value from 0.07 to 0.09 results in a decline. However, for the later duration, a higher x value from 0 to 0.09 results in a more intense afterglow (after 35 s). This is because the intensity of the afterglow is affected by trap number and trap depth. The captured electrons can easily escape from the shallower traps, contributing to the stronger afterglow. Additionally, more electrons captured by more electron traps may contribute to a stronger afterglow. Because the x = 0.07 sample has the shallowest trap depth and the more trap number compared to the samples with x smaller than 0.07, it has the most intense afterglow at the initial stage. However, because of the larger electron trap numbers, the x = 0.09 sample exhibits a more intense afterglow than that for the x = 0.07 sample at the later stage. The results show that lattice distortion caused by substituting Ba^{2+} with Sr^{2+} can enhance the afterglow intensity.

Table 1 Calculated trap depths of BGSO:Sm^{3+} (x = 0, 0.05, 0.07, 0.09).

x	T_1	T_2	Trap I depth/eV	Trap II depth/eV
0	98	139	0.742	0.824
0.05	83	121	0.712	0.788
0.07	79	115	0.704	0.776
0.09	87	118	0.720	0.782

In Fig. 6a, the change in emission peaks can be observed with increasing heating temperature. In the case of BGSO:Sm^{3+} (x = 0.07), increasing the temperature yields an enhanced emission intensity under 254-nm UV lamp irradiation. The emission intensity at 200 ˚C is more than 160% of that at room temperature and about 80% of that at room temperature at 300 ˚C (Fig. 6b). The increased emission intensities are caused by captured electrons released from electron traps that combine with the excited state of Sm^{3+} by heat processing, which compensates for the emission loss caused by thermal quenching. This phenomenon was discovered previously in our research on $ZnGa_2O_4$:Cr^{3+} persistent luminescent materials [41,42]. Fig. 6c shows the persistent luminescence decay curves for the samples after 30 s of heating at 150 ˚C. Clearly, afterglow can be seen for all samples, with more intense afterglow found at a higher x value, which is nearly the same as that without heat processing. The afterglow intensity of the x = 0.07 sample, however, exhibits the fastest decline among the samples because it has the shallowest trap depth and the electrons are emptied most easily. As a result, the afterglow of the x = 0.07 sample is highly sensitive to temperature. The BGSO:Sm^{3+} (x = 0.07) sample was placed in cylindrical containers. As shown in Fig. 6d, as the temperature rises, the phosphors exhibit increased red emission when excited by 254-nm UV light. It can be seen that the emission intensity of BGSO:Sm^{3+} (x = 0.07) is the highest at 200 ˚C. Increasing the temperature further contributes to a decrease of the red signal. The luminescence mechanism after heat processing is depicted schematically in Fig. 6e. At elevated temperatures, the trapped electrons escape to the CB and combine with the excited energy levels of Sm^{3+}, which compensates for the emission loss caused by the thermal

quenching of Sm^{3+}. As a result, the intensity of the red emission increases after heating, and the sample exhibits a temperature-dependent luminescence.

3.3. Anti-counterfeiting applications

To investigate the anti-counterfeiting application, BGSO:Sm^{3+} (x = 0.07) and $NaYF_4$:Yb^{3+}, Tm^{3+} phosphors were mixed with a mass ratio of 1:1. The PL spectra and the appearance of the mixture phosphor under 980 nm laser excitation (2.5 W) are shown in Fig. 7a. The PL spectra show several emission bands corresponding to the $^1D_2 \rightarrow {}^3H_6$ (361 nm, purple), $^1D_2 \rightarrow {}^3F_4$ (450 nm, blue), $^1G_4 \rightarrow {}^3H_6$ (473 nm, blue), $^1G_4 \rightarrow {}^3F_4$ (646 nm, red), $^3F_2 \rightarrow {}^3H_6$ (695 nm, red), and $^3F_3 \rightarrow {}^3H_6$(723 nm, red) transitions of Tm^{3+} [43]. The images show that the mixture phosphor emits a blue upconversion light. The PL spectra and appearance of the mixture phosphor obtained after excitation at 254 nm are shown in Fig. 7b. Sm^{3+} also exhibits four narrow emission peaks at 568 nm, 608 nm, 651 nm, and 707 nm. The red emission of the mixture phosphors can be seen by the naked eye. The persistent luminescence spectra of the mixture phosphor at room temperature, which is assigned to the red afterglow of Sm^{3+}, are shown in Fig. 7c. The persistent luminescence decay curve of the mixture phosphor, which was excited by a 254 nm UV lamp for 5 min, is shown in Fig. 7d. The red afterglow from the mixture phosphor lasted more than 600 seconds.

The prepared samples could be successfully employed in advanced anti-counterfeiting applications due to their different emission performances at different exciting wavelengths. To capture the emission signals of the samples under different excitation conditions, the BGSO:Sm^{3+} (x = 0.07) sample and the mixture phosphor are placed in the "B" container fabricated by metal 3D printing (Fig. 7e). The phosphor 1 is BGSO:Sm^{3+} (x = 0.07), and the phosphor 2 is a mixture of the two. Under natural light, all the patterns are white "B". The four patterns showed bright red "B" and dark red "B" emissions at 254-nm UV excitation and after removing the 254-nm UV excitation lamp, respectively (Fig. 7e). The four patterns, however, exhibited blue "B", "p", "b", and "D" under 980-nm laser excitation.

BGSO:Sm^{3+} (x = 0.07) and $SrAl_2O_4$:Eu^{2+}, Dy^{3+} phosphors were mixed with weight ratios of BGSO:Sm^{3+} (x = 0.07) to $SrAl_2O_4$:Eu^{2+}, Dy^{3+} at 200:1 and 150:1, respectively. The PL spectra of the two phosphors mixtures obtained under excitation at 254 nm are shown in Fig. 8a. The PL spectra of the two mixture phosphors show four emission peaks from Sm^{3+} at 568 nm, 608 nm, 651 nm, and 707 nm, but the emission intensity of Sm^{3+} is weaker than that before mixing. The green emission of $SrAl_2O_4$: Eu^{2+}, Dy^{3+} is visible with the broadband at 515 nm [44]. The two emission intensities for the two mixed powders were compared. The $I_{(515)}/I_{(608)}$ ratio for the mixture with the weight ratio of BGSO:Sm^{3+} (x = 0.07) to $SrAl_2O_4$:Eu^{2+}, Dy^{3+} as 200:1 is approximately 0.6. However, $I_{(515)}/I_{(608)}$ is about 1.2 for the mixture with the weight ratio of BGSO:Sm^{3+} (x = 0.07) to $SrAl_2O_4$:Eu^{2+}, Dy^{3+} as 150:1. It implies that increasing the BGSO:Sm^{3+} content would cause the emission color shifting to the red range. The persistent luminescence spectra of the two mixture phosphors are shown in Fig. 8c. In the absence of 568 nm and 707 nm emission peaks for the phosphors mixture (the weight ratio of BGSO:Sm^{3+} to $SrAl_2O_4$:Eu^{2+}, Dy^{3+} is 200:1), afterglow emission peaks at 515 nm, 608 nm and 651 nm are observed, indicating that the afterglow is yellow. The persistent luminescence spectra of the mixture phosphors (weight ratio of BGSO:Sm^{3+} to $SrAl_2O_4$:Eu^{2+}, Dy^{3+} is 150:1) only has a 515-nm peak, and the Sm^{3+} emission peak disappears, illustrating that the afterglow is green. The relative intensities of 515 nm and 608 nm at different temperatures are shown in Fig. 8d, with the weight ratio of BGSO:Sm^{3+} (x = 0.07) to $SrAl_2O_4$:Eu^{2+}, Dy^{3+} of 150:1. As the temperature rises, the intensity of the green emission peak at 515 nm decreases steadily. It is worth nothing that the red emission of the mixture increases with an increased temperature. The red emission intensity of the mixture is highest at 150 ˚C, in contrast to that of BGSO:Sm^{3+}, which has the highest intensity at 200 ˚C.

The samples were placed in cylindrical containers labeled A, B, C, and D to capture the emission signal under different excitation conditions. In each condition, sample A emits red and sample D emits green, as shown in Fig. 9. With the increased content of $SrAl_2O_4$:Eu^{2+}, Dy^{3+}, the phosphors change color from red to green under the excitation of 254-nm UV light. In contrast, samples B and C show a color change

from red to yellow after 30 seconds of excitation. After 5 min of continuous excitation with 254 nm UV light, the sample emits an afterglow that changes from red to yellow and then to green with increased content of $SrAl_2O_4:Eu^{2+}$, Dy^{3+}. Sample B's afterglow is yellow, whereas the afterglow of sample C is green. The red-light emission of samples A, B, and C increases with increasing the heating temperatures. The green emission of sample D, however, decreases gradually.

Because the mixed phosphor demonstrated time- and temperature-dependent multimode luminescence, it has great potential in advanced anti-counterfeiting applications. Here, an apple tree logo was prepared using four powders as raw materials. Fig. 10 shows the images under 254 nm UV excitation and the afterglow images at room temperature. Under the excitation of 254-nm UV light, the three apples were red and ripe. After 30 seconds of excitation, apples B and C turned yellow and immature. The afterglow of apple B was also yellow, but the afterglow of apple C turned green. Under UV excitation at 254 nm, all three apples turned bright red at 100 °C and 200 °C. The red light from three apples became stronger, while the green glow from the tree trunk became weaker. At 300 °C, the light from trunk became more weaker, while the red light from the three apples weakened but remained bright.

4. Conclusion

Red long persistent luminescent materials of $Ba_{1-x}Sr_xGa_2O_4:Sm^{3+}$ (x = 0–0.09) were synthesized using a solid-state reaction method and characterized using XRD, UV-Vis, HRTEM, SAED, TL, PLE/PL spectroscopy, and persistent luminescence decay analysis. Both Sr^{2+} and Sm^{3+} preferentially occupy the Ba^{2+} site rather than the Ga^{3+} site in $BaGa_2O_4$. Doping with Sr^{2+} and Sm^{3+} does not significantly affect the crystal structure but causes lattice shrinkage and a narrower band gap. The samples exhibit characteristic Sm^{3+} emission with emission peaks ranging from 500 nm to 750 nm, belonging to $G_{5/2}$ to the $^6H_{5/2}$ (568 nm),$^6H_{7/2}$ (608 nm), $^6H_{9/2}$ (651 nm), and $^6H_{11/2}$ (707 nm) transition of Sm^{3+}. Doping Sr^{2+} reduces the trap depth and improves red

persistent luminescence significantly. The $Ba_{0.93}Sr_{0.07}Ga_2O_4$:0.01$Sm^{3+}$ sample exhibits the brightest and strongest red afterglow. Because the escaped electrons from traps compensate for the emission loss of Sm^{3+} during the heating process, the red phosphors have unimaginably luminescent thermal stability. The emission intensity at 200 ˚C is 1.6 times that at room temperature. The prepared red persistent phosphors exhibit time- and temperature-dependent luminescence, indicating that they could be used as multimode luminescent materials in anti-counterfeiting applications. Finally, a building-block strategy for advanced anti-counterfeiting applications is proposed, using the red phosphor as an important component combined with an upconversion phosphor and a green persistent phosphor.

Acknowledgments

This work was supported in part by the Natural Science Foundation of Liaoning Province (Grant 2020-MS-081), and National Natural Science Foundation of China (Grant 51302032, 51972047, 52172112).

References

[1] Y. Li, M. Gecevicius, J. R. Qiu, Long persistent phosphors-from fundamentals to applications, Chem. Soc. Rev. 45 (8) (2016) 2090-2136.

[2] D. Poelman, D. Van der Heggen, J. R. Du, E. Cosaert, P. F. Smet, Persistent phosphors for the future: Fit for the right application, J. Appl. Phys. 128 (24) (2020) 240903.

[3] T. Maldiney, C. Richard, J. Seguin, N. Wattier, M. Bessodes, D. Scherman, Effect of core diameter, surface coating, and PEG chain length on the biodistribution of persistent luminescence nanoparticles in mice, ACS. Nano. 5 (2) (2011) 854-862.

[4] R. Fu, Y. Y. Hu, H. N. Qiao, C. L. Yang, H. Yin, M. G. Ou, Luminescence property and magnetic resonance imaging of Gd_2O_3:Tb^{3+} nanocrystals doped with Zn^{2+}, Li^{+}, Rare Met. 40 (8) (2021) 2049-2068.

[5] T. Maldiney, M. U. Kaikkonen, J. Seguin, Q. L. de Chermont, M. Bessodes, K. J. Airenne, S. Yla-Herttuala, D. Scherman, C. Richard, In vitro targeting of avidin-expressing glioma cells with biotinylated persistent luminescence nanoparticles, Bioconjug. Chem. 23 (3) (2012) 472-478.

[6] F. W. Kang, G. H. Sun, P. Boutinaud, H. Y. Wu, F. X. Ma, J. Lu, J. L. Gan, H. D. Bian, F. Gao, S. S. Xiao, Recent advances and prospects of persistent luminescent materials as inner secondary self-luminous light source for photocatalytic applications, Chem. Eng. J. 403 (2021) 126099.

[7] Z. J. Li, Y. W. Zhang, X. Wu, X. Q. Wu, R. Maudgal, H. W. Zhang, G. Han, In vivo repeatedly charging near-Infrared-Emitting mesoporous $SiO_2/ZnGa_2O_4:Cr^{3+}$ persistent luminescence nanocomposites, Adv. Sci. 2 (3) (2015) 1500001.

[8] T. Maldiney, B. T. Doan, D. Alloyeau, M. Bessodes, D. Scherman, C. Richard, Gadolinium-doped persistent nanophosphors as versatile tool for multimodal in vivo imaging, Adv. Funct. Mater. 25 (2) (2015) 331-338.

[9] J. F. Gao, J. H. Yang, X. Y. Zhang, J. Zhao, X. W. Liu, B. F. Shi, Synthesis and fluorescence properties of $CdTe:Eu^{3+}$ nanocrystals and core-shell SiO_2-coated $CdTe:Eu^{3+}$ nanospheres, Rare. Met. 38 (10) (2019), 989-995.

[10] Q. Q. Huang, H. Q. Gao, S. M. Yang, D. Ding, Z. H. Lin, Q. D. Ling, Ultrastable and colorful afterglow from organic luminophores in amorphous nanocomposites: advanced anti-counterfeiting and in vivo imaging application, Nano. Res. 13 (4) (2020) 1035-1043.

[11] T. Matsuzawa, Y. Aoki, N. akeuchi, Y. Murayama, New long phosphorescent phosphor with high brightness, $SrAl_2O_4:Eu^{2+}$, Dy^{3+}, J. Electrochem. Soc. 143 (8) (1996) 2670-2673.

[12] Y. H. Wang, L. Wang, Defect states in Nd^{3+}-doped $CaAl_2O_4:Eu^{2+}$, J. Appl. Phys. 101 (5) (2007) 053108.

[13] M. Allix, S. Chenu, E. Veron, T. Poumeyrol, E. A. Kouadri-Boudjelthia, S. Alahrache, F. Porcher, D. Massiot, F. Fayon, Considerable improvement of long-persistent luminescence in germanium and tin substituted $ZnGa_2O_4$, Chem. Mater. 25 (9) (2013) 1600-1606.

[14] A. Bessiere, S. Jacquart, K. Priolkar, A. Lecointre, B. Viana, D. Gourier, $ZnGa_2O_4:Cr^{3+}$: a new red long-lasting phosphor with high brightness, Opt. Express. 19 (11) (2011) 10131-10137.

[15] X. X. Qin, Y. Li, D. K. Wu, Y. L. Wu, R. C. Chen, Z. J. Ma, S. J. Liu, J. R. Qiu, A novel NIR long phosphorescent phosphor:$SrSnO_3:Bi^{2+}$, RSC. Adv. 5 (123) (2015) 101347-101352.

[16] C. Shi, X. Y. Shen, Y. A. Zhu, X. Q. Li, Z. Y. Pang, M. Q. Ge, Excitation wavelength-dependent dual-mode luminescence emission for dynamic multicolor anticounterfeiting, ACS. App. Mater. Inter. 11 (20) (2019) 18548-18554.

[17] D. D. Jia, Enhancement of long-persistence by Ce Co-doping in $CaS:Eu^{2+}$, Tm^{3+} red phosphor, J. Electrochem. Soc. 153 (11) (2006) H198-H201.

[18] H. M. Yang, J. Shi, M. L. Gong, A novel red emitting phosphor $Ca_2SnO_4:Eu^{3+}$, J. Solid. State. Chem. 178 (3) (2005) 917-920.

[19] L. Lin, M. Yin, C. S. Shi, W. P. Zhang, Luminescence properties of a new red long-lasting phosphor: $Mg_2SiO_4:Dy^{3+}$, Mn^{2+}, J. Alloy. Compd. 455 (1-2) (2008) 327-330.

[20] A. Mattner, L. Zimmermann, S. Lienenklaus, S. Weiss, C. Wickleder, Tailoring long lasting luminescence of red-emitting $CaWO_4:Eu^{3+}$, Sm^{3+} nanoparticles with enhanced crystallinity for improved bio-imaging, Ceram. Int. 46 (16) (2020) 26295-20298.

[21] L. Q. Yang, Z. Y. Cai, L. Q. Yang, J. Hu, Z. J. Zhao, Z. P. Liu, Solid state synthesis, luminescence and afterglow enhancements of $CaTiO_3:Pr^{3+}$ by Ga^{3+} codoping, J. Lumin. 197 (2018) 339-342.

[22] C. Rosticher, B. Viana, G. Laurent, P. Le Griel, C. Chaneac, Insight into $CaMgSi_2O_6:Eu^{2+}$, Mn^{2+}, Dy^{3+} nanoprobes: influence of chemical composition and crystallinity on persistent red luminescence, Eur. J. Inorg. Chem. (22) (2015) 3681-3687.

[23] J. Zhang, G. B. Chen, A long-persistent phosphor $Sr_3MgSi_2O_{8-1.5x}N_x:Eu^{2+}$, Dy^{3+}, Mn^{2+} based on white LEDs applications, J. Lumin. 211 (2019) 69-75.

[24] S. Ye, J. H. Zhang, X. Zhang, S. Z. Lu, X. G. Ren, X. J. Wang, Mn^{2+} activated red phosphorescence in $BaMg_2Si_2O_7:Mn^{2+}$, Eu^{2+}, Dy^{3+} through persistent energy transfer, J. Appl. Phys. 101 (6) (2007) 063545.

[25] Z. H. Ju, R. P. Wei, J. R. Zheng, X. P. Gao, S. H. Zhang, W. S. Liu, Synthesis and phosphorescence mechanism of a reddish orange emissive long afterglow phosphor Sm^{3+}-doped Ca_2SnO_4, Appl. Phys. Lett. 98 (12) (2011) 121906.

[26] B. F. Lei, Y. L. Liu, G. B. Tang, Z. R. Ye, C. S. Shi, A new orange-red long-lasting phosphor material $Y_2O_2S:Sm^{3+}$, Chem. J. Chinese U. 24 (2) (2003) 208-210.

[27] X. Yu, X. H. Xu, J. B. Qiu, Enhanced long persistence of $Sr_2SnO_4:Sm^{3+}$ red phosphor by co-doping with Dy^{3+}, Mater. Res. Bull. 46 (4) (2011) 627-629.

[28] Z. H. Wang, X. F. Shi, X. J. Wang, Q. Zhu, X. D. Li, B. N. Kim, X. D. Sun, J. G. Li, Enhanced hydrothermal crystallization and color tailorable photoluminescence of hexagonal structured YPO_4:Sm/Tb nanorods, Crys. Eng. Comm. 20 (17) (2018) 2357-2365.

[29] Y. Zhang, R. Huang, H. L. Li, D. J. Hou, Z. X. Lin, J. Song, Y. Z. Guo, H. H. Lin, C. Song, Z. W. Lin, J. Robertson, Germanium substitution endowing Cr^{3+}-doped zinc aluminate phosphors with bright and super-long near-infrared persistent luminescence, Acta. Mater. 155 (2018) 214-221.

[30] H. M .Li, J. Z. Cai, R. Pang, G. Y. Liu, S. Zhang, L. H. Jiang, D.Li, C. Y. Li, J. Feng, H. J. Zhang, J. A strategy for developing thermal-quenching-resistant emission and super-long persistent luminescence in $BaGa_2O_4:Bi^{3+}$, Mater. Chem. C. 2019, 7 (42) (2019) 13088-13096.

[31] H. M. Li, H. Y. Wu, R. Pang, G. Y. Liu, S. Zhang, L. H. Jiang, D. Li, C. Y. Li, J. Feng, H. J. Zhang, Investigation on the photoluminescence and thermoluminescence of $BaGa_2O_4:Bi^{3+}$ at extremely low temperatures, J. Mater. Chem. C. 9 (5) (2021) 1786-1793.

[32] V. Kahlenberg, R. X. Fischer, J. B. Parise, The stuffed framework structure of $BaGa_2O_4$, J. Solid. State. Chem. 154 (2) (2000) 612-618.

[33] L. L. Noto, D. Poelman, V. R. Orante-Barron, H. C. Swart, L. E. Mathevula, R. Nyenge, M. Chithambo, B. M. Mothudi, M. S. Dhlamini, Photoluminescence and thermoluminescence properties of $BaGa_2O_4$, Physica. B. 535 (2018) 268-271.

[34] X. Q. Zhou, G. F. Ju, T. S. Dai, Y. Li, H. Y. Wu, Y. H. Jin, Y. H. Hu, Strontium substitution enhancing a novel Sm^{3+}-doped barium gallate phosphor with bright and red long persistent luminescence, J. Lumin. 218 (2020) 8.

[35] H. Lin, D. L. Yang, G. S. Liu, T. C.Ma, B. Zhai, Q. D. An, J. Y. Yu, X. J. Wang, X. R. Liu, E. Y. B. Pun, Optical absorption and photoluminescence in Sm^{3+}- and Eu^{3+}-doped rare-earth borate glasses, J. Lumin. 2005, 113 (1-2) (2005) 121-128.

[36] J. X. Wang, Y. Xie, J. L. Guo, X. M. Yao, X. Geng, J. Gao, X. Y. Feng, Z. J. Zhou, Y. Y. Liu, B. Deng, R. J. Yu, Abnormal thermal quenching behavior and optical properties of a novel apatite-type $NaCa_3Bi(PO_4)_3F:Sm^{3+}$ orange-red-emitting phosphor for w-LED applications, Ceram. Int. 47 (20) (2021) 28167-28177.

[37] T. Wang, W. J. Bian, D. C. Zhou, J. B. Qiu, X. Yu, X. H. Xu, Red long lasting phosphorescence in $Ca_2Ge_7O_{16}:Sm^{3+}$ via persistent energy transfer from the host to Sm^{3+}, Mater. Res. Bull. 74 (2016) 151-155.

[38] M. H. Wu, S. Y. Liu, Y. C. Sun, W. Chen, L. F. Huang, G. L. Chen, Z. S. Zheng, Energy transfer of wide band long persistent phosphors of Sm^{3+}-Doped $ZrSiO_4$, Mater. Chem. Phys. 251 (2020) 123086.

[39] K. Van den Eeckhout, P. F. Smet, D. Poelman, Persistent luminescence in Eu^{2+}-doped compounds: A Review. Materials. 3 (2010) 2536.

[40] J. Xu, S. Tanabe, Persistent luminescence instead of phosphorescence: History, mechanism, and perspective, J. Luimn. 205 (2019) 581-620.

[41] J. Q. Xiahou, Q. Zhu, L. Zhu, S. Huang, T. Zhang, X. D, Sun, J. G. Li, Lattice-site engineering in $ZnGa_2O_4:Cr^{3+}$ through Li^+ doping for dynamic luminescence and advanced optical anti-counterfeiting, J. Mater. Chem. C. 10 (2022) 7935-7948.

[42] T. Si, Q. Zhu, T. Zhang, X. D. Sun, J. G. Li, Co-doping Mn^{2+}/Cr^{3+} in $ZnGa_2O_4$ to fabricate chameleon-like phosphors for multi-mode dynamic anti-counterfeiting, Chem. Eng. J. 426 (2021) 131744.

[43] H. Suo, C. Guo, Z. Yang, S. Zhou, C. Duan, M. Yin, Thermometric and optical heating bi-functional properties of upconversion phosphor $Ba_5Gd_8Zn_4O_{21}:Yb^{3+}/Tm^{3+}$, J. Mater. Chem. C. 3 (28) (2015) 7379-7385.

[44] Hai, M. K. Pei, Q. Ren, X. L. Wu, E. L. Yang, D. Xu, J. F. Zhu, Ag nanoparticles significantly improve the slow decay brightness of $SrAl_2O_4:Eu^{2+}$, Dy^{3+} by the surface plasmon effect, Dalton. T. 51 (6) (2022) 2287-2295.

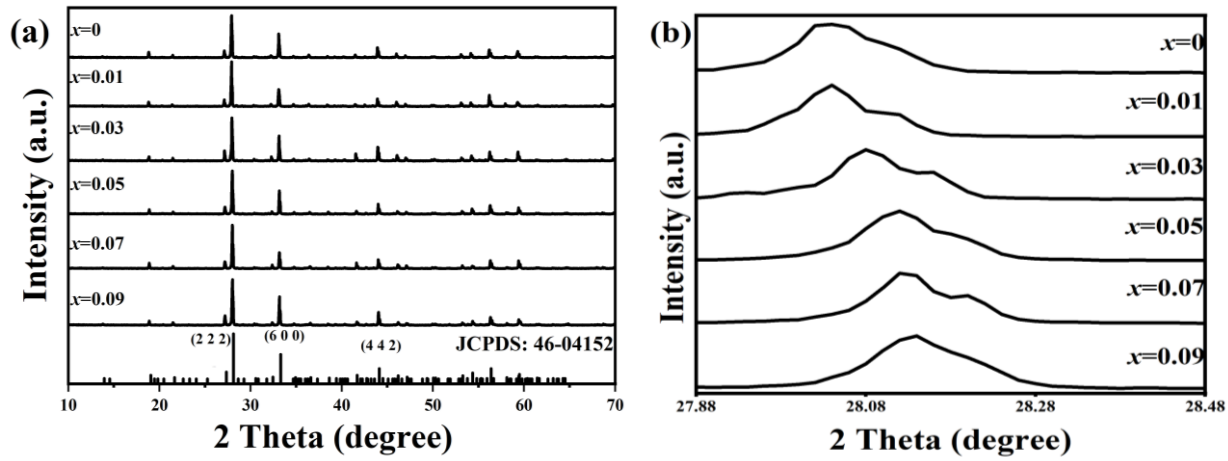

Fig. 1. (a) X-ray diffraction patterns and (b) enlarged (222) diffraction of BGSO:Sm^{3+} (x = 0- 0.09).

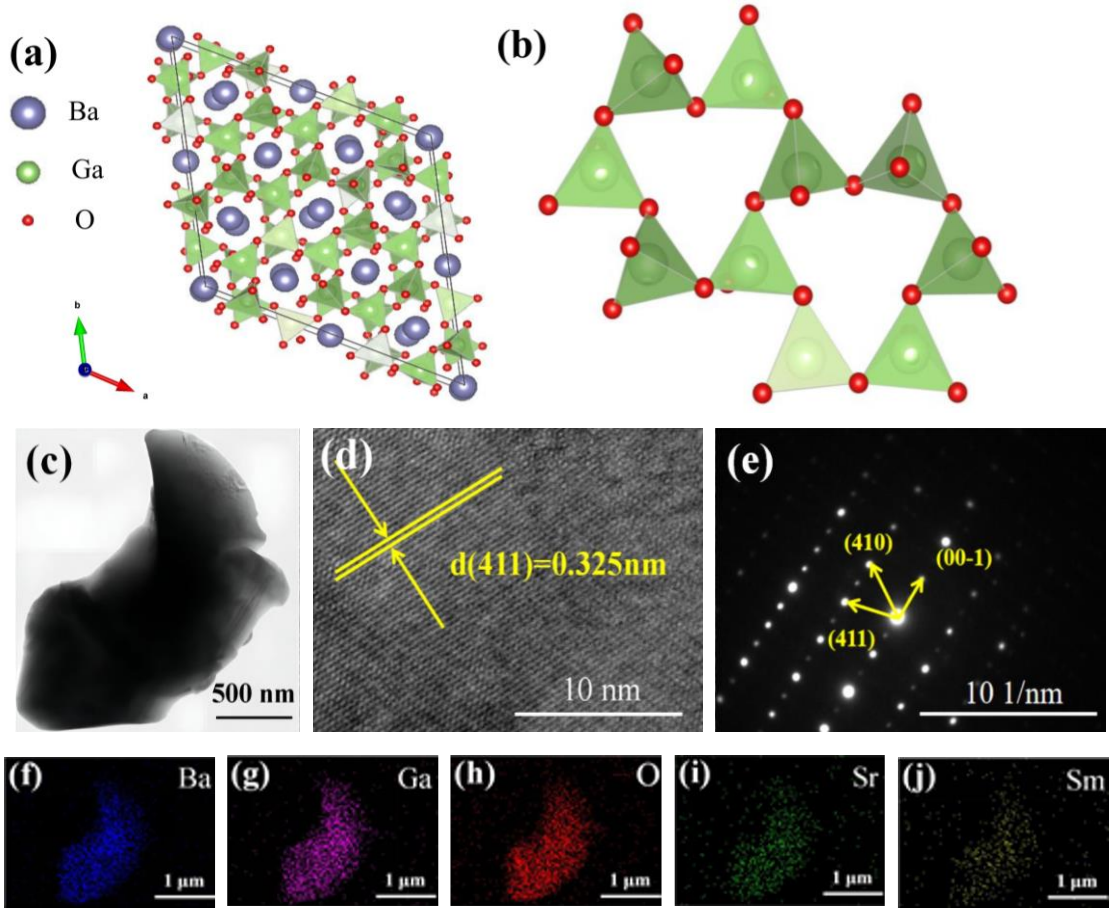

Fig. 2. (a) Crystal unit cell of $BaGa_2O_4$ viewed along the c-axis, (b) two different types of six-membered rings consisted of Ga-O tetrahedron, (c) TEM image, (d) HR-TEM image, (e) SAED pattern, and (f-j) element distribution of BGSO:Sm^{3+} (x = 0.07).

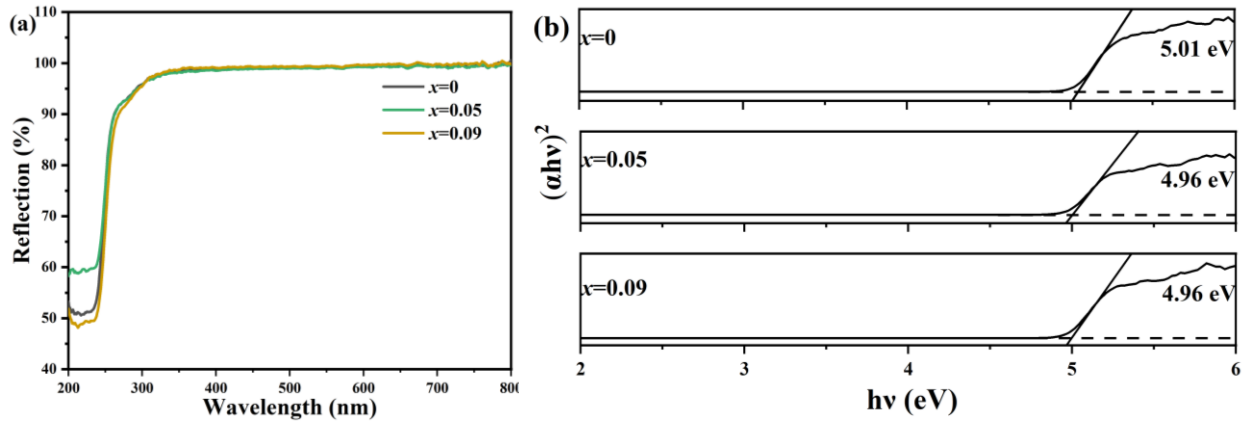

Fig. 3. (a) Diffuses reflection spectra and (b) the bandgap energies of the BGSO (x = 0, 0.05, 0.09).

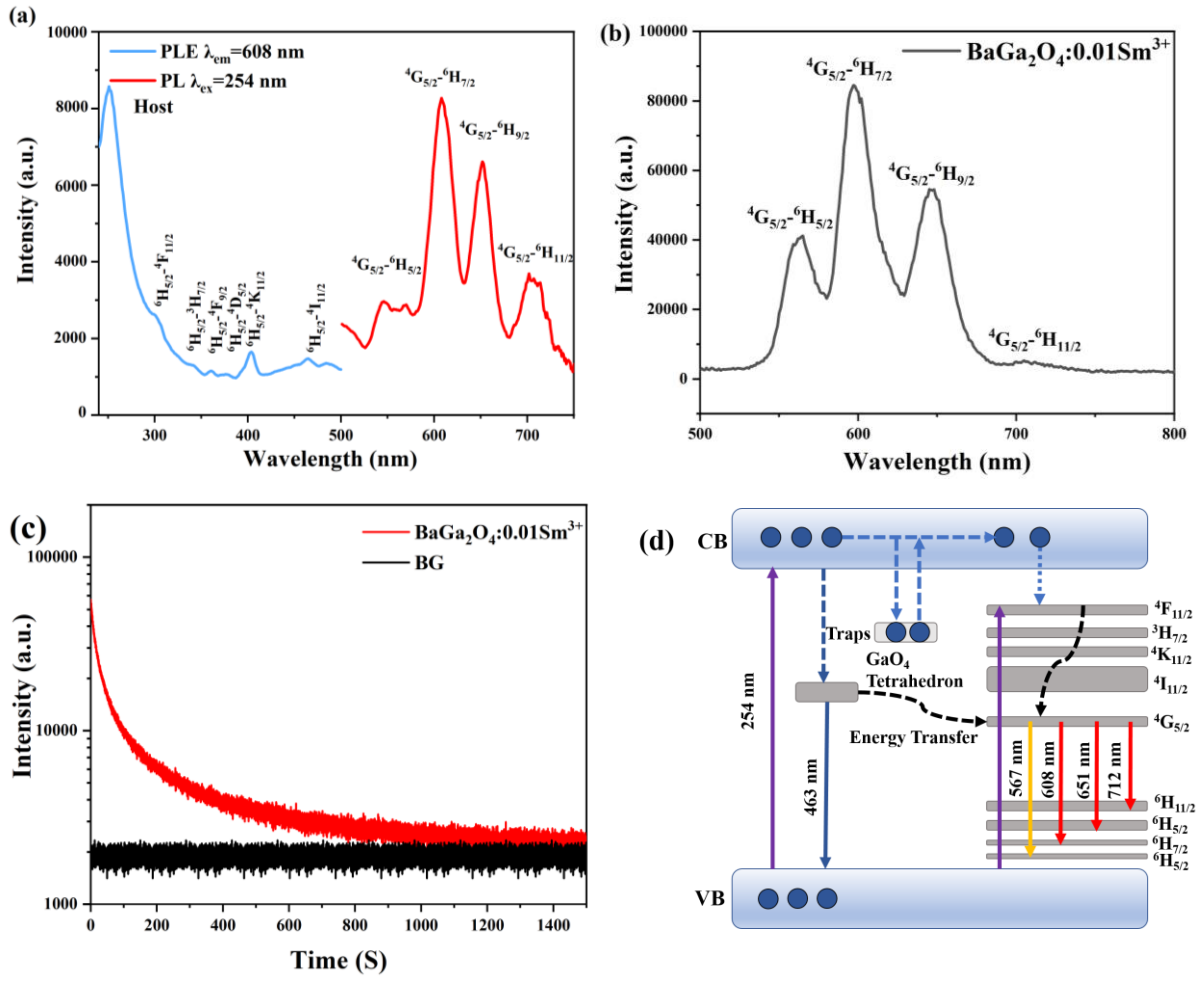

Fig. 4. (a) PLE and PL spectra, (b) persistent luminescence spectra, (c) persistent luminescence decay curve of $BaGa_2O_4$:0.01Sm^{3+}, and (d) schematic illustration of the luminescence mechanism for $BaGa_2O_4$:0.01Sm^{3+}.

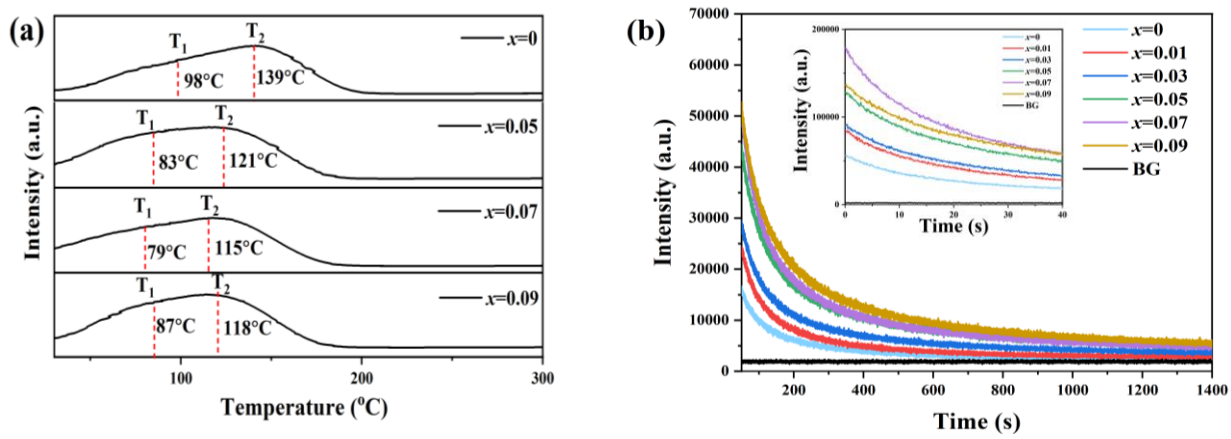

Fig. 5. (a) TL glow curves for BGSO:Sm^{3+} (x = 0, 0.05, 0.07, 0.09) and (b) the persistent luminescence decay curves (monitored at 608 nm after 254-nm UV light illumination for 5 min).

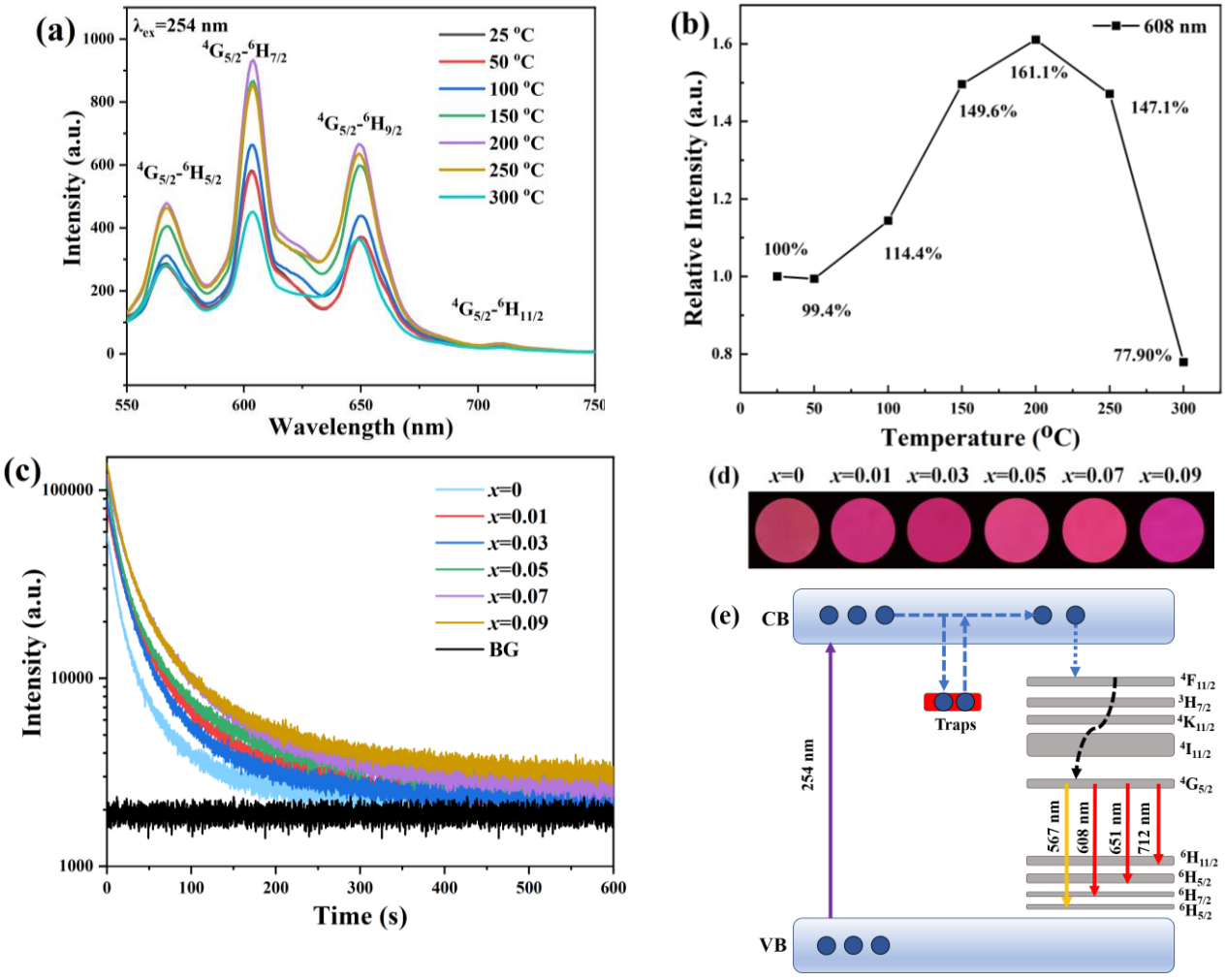

Fig. 6. (a) PL spectra of BGSO:Sm^{3+} (x = 0.07) at different temperatures, (b) the relative intensities of 608 nm at different temperatures for BGSO:Sm^{3+} (x = 0.07), (c) persistent luminescence decay curves of BGSO:Sm^{3+} (x = 0-0.09) after heating at 150 ^{o}C, (d) appearances of BGSO:Sm^{3+} (x = 0.07) phosphors at different temperatures

under 254 nm light excitation, and (e) schematic illustration of the luminescence mechanism for BGSO:Sm^{3+} after heat processing.

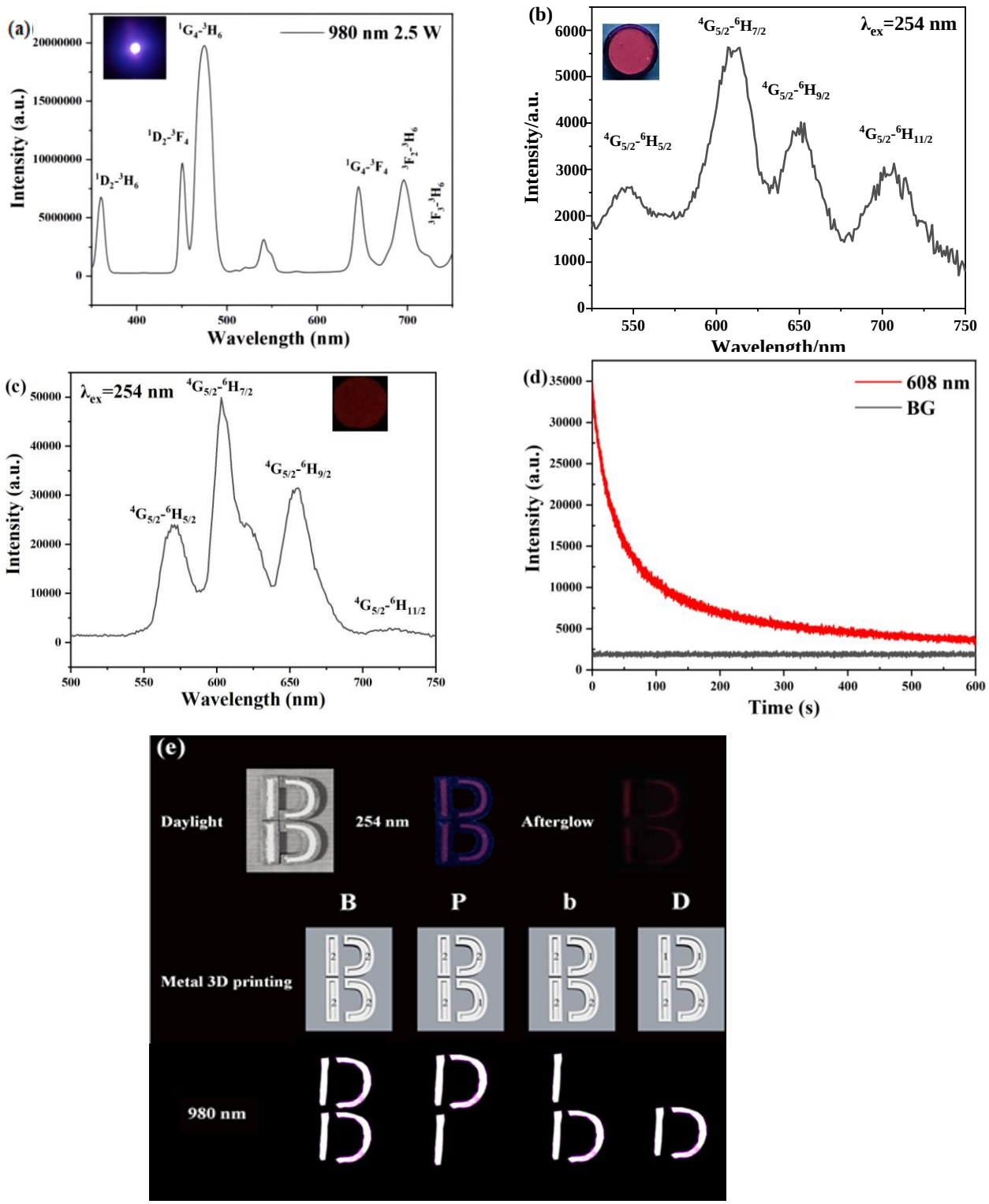

Fig. 7. PL spectra and the appearance of the mixture phosphor (a) under 980 nm laser excitation (2.5 W) and (b) under 254-nm UV light excitation, respectively. (c) and (d) are the persistent luminescence spectra and the afterglow and the persistent

luminescence decay curves of the mixture phosphor. The mixture phosphor is composed of $Ba_{0.93}Sr_{0.07}Ga_2O_4$:0.01$Sm^{3+}$ and $NaYF_4$:Yb^{3+},Tm^{3+} with the weight ratio of 1:1. (e) is the designed logo for anti-counterfeiting application, with phosphor 1 as $Ba_{0.93}Sr_{0.07}Ga_2O_4$:0.01$Sm^{3+}$ and phosphor 2 as the mixture phosphor.

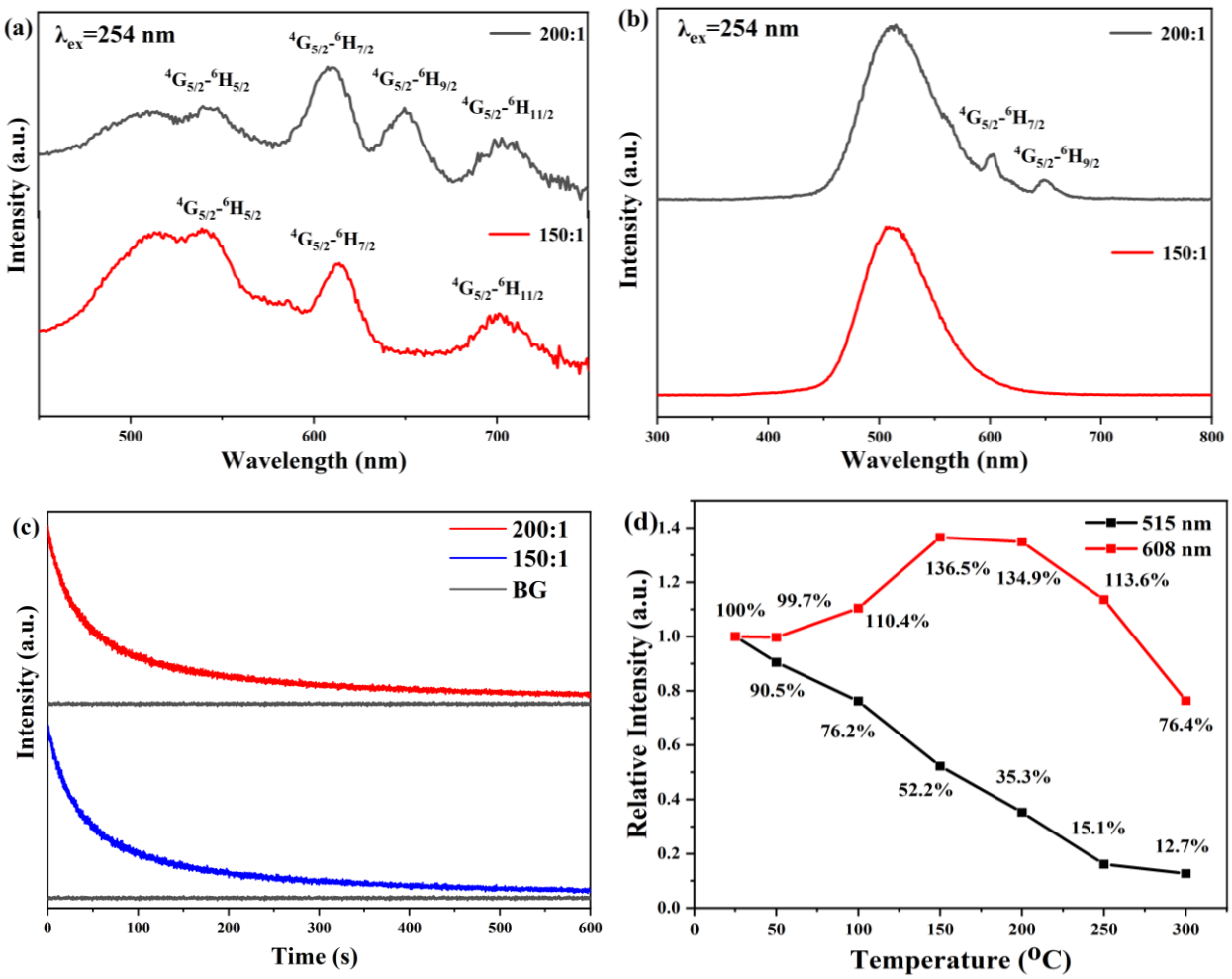

Fig. 8. (a) PL spectra, (b) the persistent luminescence spectra, and (c) persistent luminescence decay curves of two typical mixture phosphors, with the weight ratio of $Ba_{0.93}Sr_{0.07}Ga_2O_4$:0.01$Sm^{3+}$ to $SrAl_2O_4$:Eu^{3+}, Dy^{3+} as 200:1 and 150:1, respectively. (d) is the relative intensities of 515 nm and 608 nm at different temperatures for the mixtures, with the weight ratio of $Ba_{0.93}Sr_{0.07}Ga_2O_4$:0.01$Sm^{3+}$ to $SrAl_2O_4$:Eu^{3+}, Dy^{3+} as 150:1.

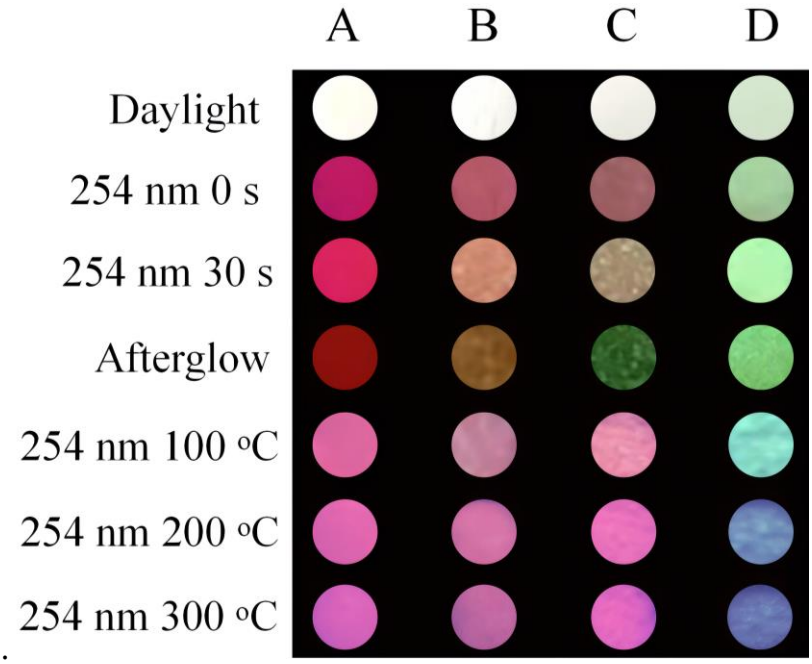

Fig. 9. Appearances of four typical samples under daylight, 254 nm UV light for 0s and 30 s at different temperatures, and the afterglows after removing the UV light source. Sample A is $Ba_{0.93}Sr_{0.07}Ga_2O_4$:0.01$Sm^{3+}$ and sample D is the mixture of $BaSO_4$ and $SrAl_2O_4$:Eu^{3+}, Dy^{3+} (the weight ratio is 100:1). The weight ratio of $Ba_{0.93}Sr_{0.07}Ga_2O_4$:0.01$Sm^{3+}$ to $SrAl_2O_4$:Eu^{3+}, Dy^{3+} is 200:1, 150:1 for samples B and C respectively.

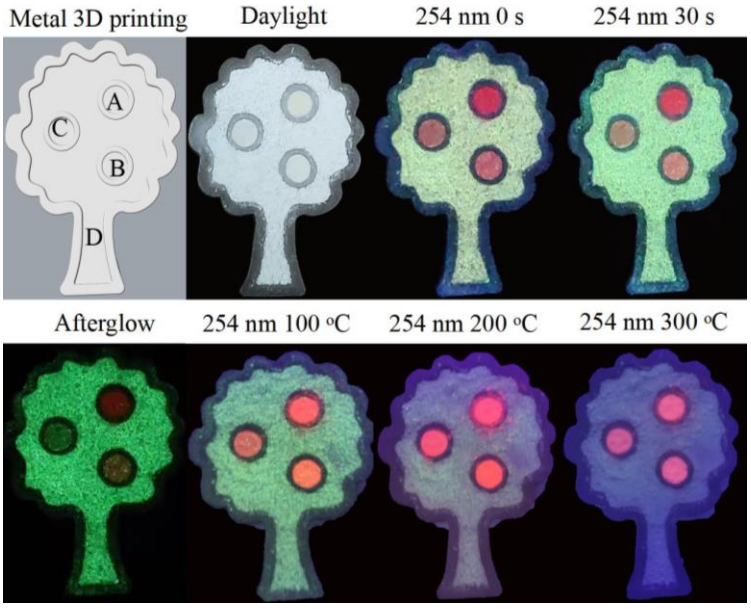

Fig. 10. Appearances of the signals for the pattern of "apple tree" with four typical samples placed in the designed container fabricated by metal 3D printing.

Supporting Information

A building-block strategy for dynamic anti-counterfeiting by using $(Ba,Sr)Ga_2O_4:Sm^{3+}$ new red persistent luminescent phosphor as an important component

Ao Guo[a], Qi Zhu[a,*], Shimeng Zhang[a], Xudong Sun[b] and Ji-Guang Li[c,*]

[a]*Key Laboratory for Anisotropy and Texture of Materials (Ministry of Education), School of Materials Science and Engineering, Northeastern University, Shenyang, Liaoning 110819, China*

[b]*Foshan Graduate School of Northeastern University, Foshan, Guangdong 528311, PR China*

[c]*Research Center for Functional Materials, National Institute for Materials Science, Namiki 1-1, Tsukuba, Ibaraki 305-0044, Japan*

*E-mail: zhuq@smm.neu.edu.cn and LI Jiguang@nims.go.jp

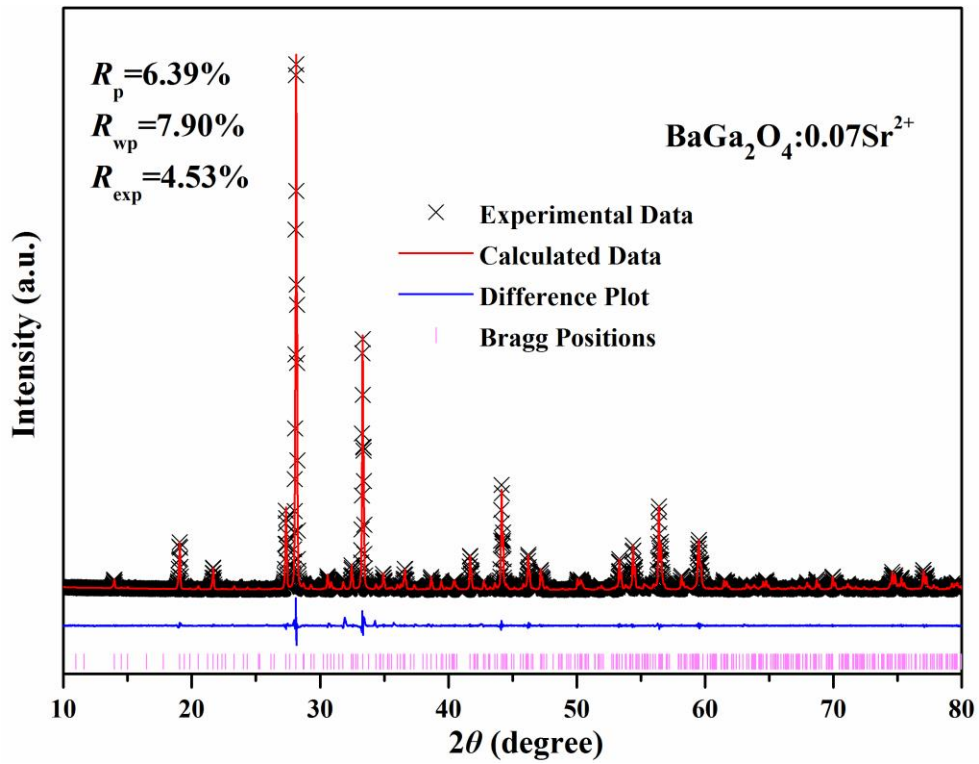

Figure S1. Rietveld refinements of BGSO (x=0.07 sample).

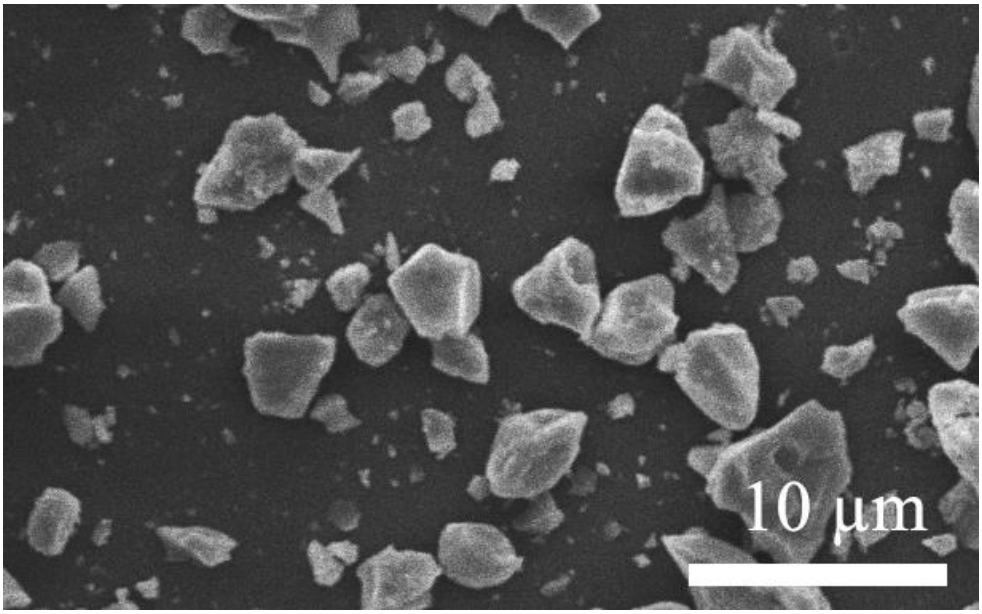

Figure S2. FE-SEM image of BGSO:Sm^{3+} (x = 0.07) powder.

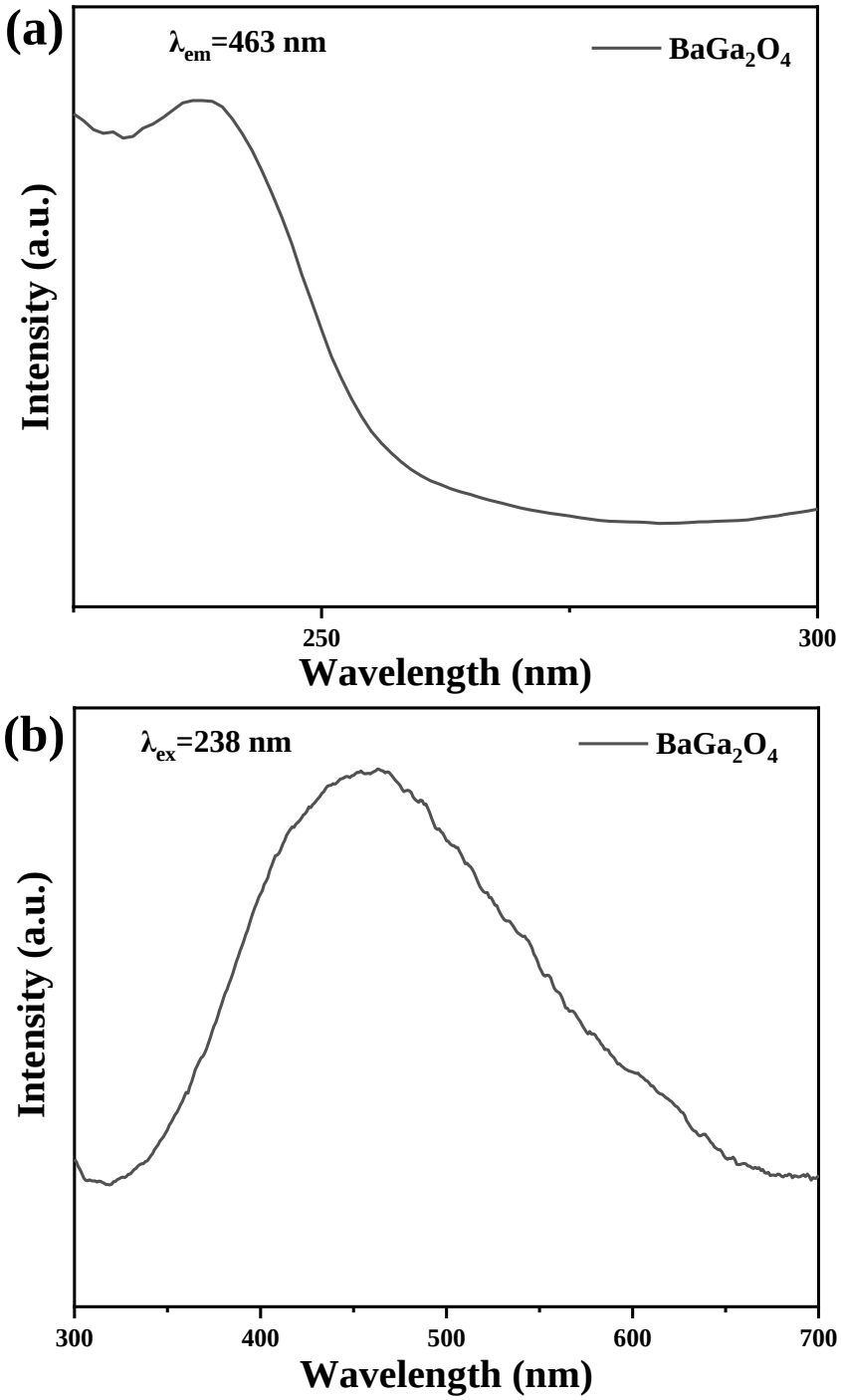

Figure S3. (a) PLE spectra and (b) PL spectra of $BaGa_2O_4$.

Declaration of Interest Statement

There are no conflicts of interest to declare.